Signal-background interference for digluon resonances at the Large Hadron Collider

Prudhvi N. Bhattiprolu and Stephen P. Martin

Department of Physics, Northern Illinois University, DeKalb IL 60115

We study the interference between the amplitudes for $gg \to X \to gg$, where X is a new heavy digluon resonance, and the QCD background $gg \to gg$, at the Large Hadron Collider. The interference produces a large low-mass tail and a deficit of events above the resonance mass, compared to the naive pure resonance peak. For a variety of different resonance quantum numbers and masses, we evaluate the signal-background interference contribution at leading order, including showering, hadronization, and detector effects. The resulting new physics dijet mass distribution may have a shape that appears, after QCD background fitting and subtraction, to resemble an enhanced peak, a shelf, a peak/dip, or even a pure dip. We argue that the true limits on new digluon resonances are likely to differ significantly from the limits obtained when interference is neglected, especially if the branching ratio to gg is less than 1.

Contents

I. INTRODUCTION

Understanding the dijet invariant mass spectrum provides an essential way to discover or set limits on certain types of new physics beyond the Standard Model (SM), as new particles could decay primarily to gg, $q\bar{q}$, qq, or qg. The most recent Large Hadron Collider (LHC) searches in the dijet channel can be found in [1, 2] (CMS) and [3, 4] (ATLAS), based in part on strategies developed in earlier searches in [5]-[11]. Some models of phenomenological interest that yield dijet signals include the following. Chiral color [12–18], flavor-universal coloron [19–30], and certain supersymmetric models [31] predict the existence of massive color-octet gauge bosons, because of the embedding of QCD within a broken symmetry of $SU(3) \times SU(3)$ gauge group beyond the TeV scale. These massive gauge bosons are known as axigluons (axial-vectors) or colorons (vectors), which typically decay to a $q\bar{q}$ pair, or topgluons [32–36], which can preferentially couple to t quarks and appear in topcolor and similar models of dynamical electroweak symmetry breaking. Some E_6 grand unified theories predict diquarks [37] which decay to qq. Models with new electroweak gauge bosons W' and Z' [38, 39], on top of the Standard Model, could also decay to a $q\bar{q}$ pair. Excited or composite quarks [40, 41] could decay to qg or $\bar{q}g$. String Regge resonances [42, 43] of the quark and the gluon could decay to a quark and a gluon. Scalar color-octets, which occur in models of technicolor [44], and universal extra dimensions [45, 46], can be considered as digluon resonances. The Randall-Sundrum (RS) model [47], which provides a possible solution to the Planck scale hierarchy problem by adding extra dimensions, predicts RS gravitons which decay to gluon pairs or quark pairs. The Kaluza-Klein (KK) states interact with the Standard Model fields, thus the KK gravitons could contribute to the dijet spectrum [48]. Also, models with dark matter mediators [49–52] which also couple to quarks, predict dijet signatures. A general classification and study of dijet resonances for the LHC has been given in [53].

One of the biggest challenges in limiting or discovering a new dijet resonance is dealing with the huge QCD background, which is imperfectly known but should be a smooth function of the invariant mass in the range appropriate for new physics searches. In order to effectively deal with the background, for lower masses CMS uses the data scouting [54] technique to reconstruct or save only the crucial information to do analyses, thus allowing them to record more events. In the CMS and ATLAS searches that set limits on dijet resonances, the interference between the resonant amplitude and the QCD background was not considered, which could have a significant impact on the experimental limits. As we will see below, the interference effect means that dijet resonances need not necessarily produce a peak in the dijet mass distributions in the vicinity of their mass, especially once the QCD background fitting and subtraction are implemented. The effects of interference are likely to be most pronounced in the digluon channel, where the QCD background amplitudes are large compared to the new-physics amplitudes. A preliminary study of this kind of interference effect for digluon resonances, done only at parton level with smearing and only for the case of a spin-0 color-singlet with mass near 750 GeV (motivated in large part by an infamous possible diphoton signal that turned out to be a fluctuation), was performed in ref. [55].

A similar, but much smaller, effect on the diphoton lineshape for the Higgs boson due

to interference with the quark-loop induced Standard Model amplitudes $gg \to \gamma\gamma$ has been studied in refs. [56]-[65]. As noted in [58], there is a shift in the diphoton mass peak which can eventually be observable, and can be used [61] to bound the Higgs boson width. Another important case of interference involving Standard Model Higgs boson-mediated amplitudes and the continuum contributions occur for the processes $gg \to ZZ$ and $gg \to W^+W^-$, which have been studied in refs. [66–87]. In particular, as noted in [74], enhanced contributions occur for invariant masses far off the Higgs mass-shell, despite its narrow width, and are reduced by the interference. This effect can be, as shown in [77, 78] (see refs. [79–87] for further important developments), and has been [88–93], used to bound the Higgs width from studying VV events in the invariant mass region far above the Higgs mass at the LHC. Other aspects of resonance-continuum interferences as a probe of new physics at the LHC, with approaches similar or complementary to the present paper, have been given in [94–100]. Also, reference [101] discussed the importance of non-interference off-shell effects in spin-1 digluon resonances at hadron colliders.

In this paper, we consider digluon resonances of various spin and color quantum numbers, whose existence need not necessarily be justified by any particular model. We study the importance of the interference between the digluon resonant signal $gg \to X \to gg$ and the QCD background $gg \to gg$ when setting limits on the digluon resonances, where X couples to gluon pairs by non-renormalizable operators, subject to QCD gauge invariance. Here and from now on, X refers to any such digluon resonance.

At leading order (LO) the interference terms change the naive Breit-Wigner resonance peak, at dijet invariant mass close to the resonance mass ($m_{jj} \approx M_X$), to a peak just below and a dip just above the resonance mass. (As a caution, we note that a next-to-leading order (NLO) calculation with virtual 1-loop and real emission of an extra jet would provide a more realistic estimate; NLO effects can be quite significant for the interference in the analogous case of diphoton Higgs signal/background interference [59]-[62], especially when there is an additional jet with high p_T.) The magnitude of these interference effects are dependent on the spin and the color structures of the digluon resonances. The interference effects are studied for scalar and pseudo-scalar resonances in both singlet and octet color representations, spin-1 color-octets, and color-singlet massive gravitons. Although the Landau-Yang theorem forbids the decay of a massive spin-1 particle into two on-shell photons, it does not forbid the decay of an odd parity massive color-octet spin-1 particle into a pair of on-shell gluons in a non-Abelian $SU(N_c)$ Yang-Mills theory [23, 102–105], as in our case.[†]

The previous study [55] mentioned above for a 750 GeV color-singlet spin-0 digluon resonance used parton-level differential cross-sections which were then smeared by convolution with an assumed approximate detector response function. Here, we repeat that type of analysis, but also obtain the detector-level dijet invariant mass distributions for both the signal process alone, and its interference with the QCD background using Monte Carlo event gen-

---

[†] The Landau-Yang theorem also rules out the possibility of colored or colorless massive pseudo-vectors (i.e. even-parity spin-1 particles) decaying to a pair of on-shell massless gauge bosons. In general, this selection rule does not forbid the decay of a massive spin-1 particle to two massless gauge bosons if one of the three bosons is off-shell [104, 105].

erators including showering and hadronization and detector simulation. The latter method serves as a validation of the qualitative results obtained by the simpler method used in ref. [55].

The rest of this paper is structured as follows. In Section II, we introduce the considered models of various spin and color quantum numbers, along with their effective interaction Lagrangians. To elucidate the importance of the interference effects, we then consider a few benchmark examples for various resonance masses $M_X = (750, 1000, 1500, 2000, 2500, 3000)$ GeV, such that their resonant production cross sections are close to the present claimed exclusions of the CMS experiment as given in the most recent reported searches [1, 2]. In Section III, we discuss the methods and techniques used to obtain smeared parton-level and full event simulated results. We then present the results for the considered benchmark models in section IV. We start by assuming that X almost always decays to a pair of gluons. We then show in section V that the interference effects are even more dramatic if the digluon resonance has other non-detectable decays contributing to its width. (These could include invisible or multi-jet final states from each X decay.) Finally, in Section VI, we conclude the paper by summarizing the significance of the signal/background interference for digluon resonances.

II. DIGLUON RESONANCES AND BENCHMARK MODELS

The models considered in this paper are described in the following. In all the models, X is assumed to couple to gluons with non-renormalizable operators invariant under QCD gauge transformations. The couplings c_i are dimensionless, possibly complex, form factors, and Λ is a mass scale associated with new physics. The effective form-factor couplings will be suppressed by masses of heavier particles, if the interaction is loop-induced.

Spin 0, color singlet: The effective Lagrangian for an even parity (scalar) resonance X can be written as:

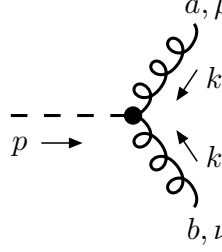$$\mathcal{L} = \frac{c_1}{2\Lambda} X F^a_{\mu\nu} F^{a\mu\nu}, \tag{2.1}$$

and for an odd parity (pseudo-scalar) resonance as:

$$\mathcal{L} = -\frac{c_2}{4\Lambda} X \epsilon^{\mu\nu\rho\sigma} F^a_{\mu\nu} F^a_{\rho\sigma}, \tag{2.2}$$

where $F^a_{\mu\nu} = \partial_\mu A^a_\nu - \partial_\nu A^a_\mu - g_s f^{abc} A^b_\mu A^c_\nu$ is the QCD field strength tensor for $a, b, c = 1, 2, \ldots, 8$, and f^{abc} are the anti-symmetric structure constants of $SU(3)_c$, and g_s is the strong coupling constant. The corresponding Feynman rules for X-g-g couplings, for both color-singlet scalar and pseudo-scalar, are shown in Figure 2.1.

Spin 0, color octet: The effective Lagrangian for an even parity (scalar) resonance X is:

$$\mathcal{L} = \frac{c_3}{2\Lambda} d^{abc} X^c F^a_{\mu\nu} F^{b\mu\nu}, \tag{2.3}$$
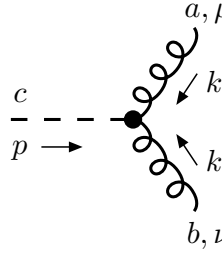
$$-i\frac{2c_1}{\Lambda}\delta^{ab}(k_1\cdot k_2\,\eta^{\mu\nu} - k_2^\mu k_1^\nu) \qquad \text{(scalar)}$$

$$-i\frac{2c_2}{\Lambda}\delta^{ab}\epsilon^{\mu\nu\rho\sigma}k_{1\rho}k_{2\sigma} \qquad \text{(pseudo-scalar)}$$

FIG. 2.1: Feynman rule for the effective coupling of parity-even (top) and parity-odd (bottom) spin-0 color-singlet resonance with a gluon pair, with $p^\mu + k_1^\mu + k_2^\mu = 0$. Here, c_1 and c_2 are dimensionless form factors, and Λ is the mass scale associated with the new physics.

$$-i\frac{2c_3}{\Lambda}d^{abc}(k_1\cdot k_2\,\eta^{\mu\nu} - k_2^\mu k_1^\nu) \qquad \text{(scalar)}$$

$$-i\frac{2c_4}{\Lambda}d^{abc}\epsilon^{\mu\nu\rho\sigma}k_{1\rho}k_{2\sigma} \qquad \text{(pseudoscalar)}$$

FIG. 2.2: Feynman rule for the effective coupling of parity-even (top) and parity-odd (bottom) spin-0 color-octet resonance with a gluon pair, with $p^\mu + k_1^\mu + k_2^\mu = 0$. Here, c_3 and c_4 are dimensionless form factors, and Λ is the mass scale associated with the new physics.

and for an odd parity (pseudo-scalar) resonance it is:

$$\mathcal{L} = -\frac{c_4}{4\Lambda}d^{abc}X^c\epsilon^{\mu\nu\rho\sigma}F_{\mu\nu}^a F_{\rho\sigma}^b, \tag{2.4}$$

where the symmetric anomaly coefficients of $SU(3)_c$ are defined as:

$$d^{abc} = 2\text{Tr}[\{T^a, T^b\}T^c], \tag{2.5}$$

with the usual normalization for the fundamental representation matrices

$$\text{Tr}[T^a T^b] = \frac{1}{2}\delta^{ab}, \tag{2.6}$$

so that

$$d^{abc}d^{abe} = \frac{N_c^2 - 4}{N_c}\delta^{ce} = \frac{5}{3}\delta^{ce}. \tag{2.7}$$

The corresponding Feynman rules for the effective couplings of color-octet scalar and pseudo-scalar with two gluons are shown in Figure 2.2.

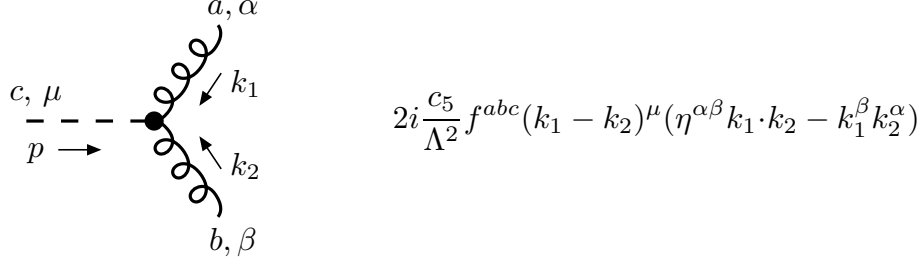$$2i\frac{c_5}{\Lambda^2}f^{abc}(k_1-k_2)^\mu(\eta^{\alpha\beta}k_1\cdot k_2 - k_1^\beta k_2^\alpha)$$

FIG. 2.3: Feynman rule for the effective coupling of a spin-1 color-octet resonance with a gluon pair, with $p^\mu + k_1^\mu + k_2^\mu = 0$. Here, c_5 is a dimensionless form factor, and Λ is the mass scale associated with the new physics.

Spin 1, color octet: The Landau-Yang theorem does not forbid the decay of a color-octet massive vector to an on-shell gluon pair [23, 102–105]. The effective Lagrangian describing the non-trivial coupling of two gluons to a massive odd-parity spin-1, color-octet resonance X_μ^a is [104]:

$$\mathcal{L} = \frac{c_5}{\Lambda^2}f^{abc}(D_\mu X_\nu^a - D_\nu X_\mu^a)F^{b\nu\rho}F_\rho^{c\mu} \tag{2.8}$$

where D_μ is the gauge-covariant derivative. (For the X-gluon-gluon interaction, only the ordinary partial derivative part of this is pertinent, so one can replace D_μ by ∂_μ.) Note that dimensional analysis says that if we want c_5 to be dimensionless, we now need Λ^2 in the denominator, where Λ is the new physics scale. The Feynman rule for a massive color-octet vector coupling to a gluon pair is shown in Figure 2.3. In the Feynman rule, the contributions proportional to k_1^α and k_2^β have been dropped, as they never contribute to amplitudes because of $\epsilon_1 \cdot k_1 = \epsilon_2 \cdot k_2 = 0$. It should be noted that our treatment of the spin-1 color-octet is not the same as that of the usual "axigluon/coloron" models as in [12, 20, 23]. In those models, the spin-1 color-octet appears primarily as a $q\bar{q}$ resonance; although the gg production channel is non-zero, in specific models it is small compared to the $q\bar{q}$ production channel. In this paper, we instead focus on the case that the production of the resonance is mostly through a large coupling to gg.

Spin 2, color singlet: The free Lagrangian for a massive spin-2 resonance $X^{\mu\nu}$, first derived by Markus Fierz and Wolfgang Pauli, can be written as [106]:

$$\mathcal{L}_f = \frac{1}{2}X^{\mu\nu}\partial_\alpha\partial^\alpha X_{\mu\nu} - X^{\mu\nu}\partial_\mu\partial^\alpha X_{\nu\alpha} + X\partial_\mu\partial_\nu X^{\mu\nu} - \frac{1}{2}X\partial_\mu\partial^\mu X$$
$$+ \frac{1}{2}M_X^2\left[X^{\mu\nu}X_{\mu\nu} - X^2\right], \tag{2.9}$$

where $X = X_\alpha^\alpha$.

The effective interaction Lagrangian for an even parity color-singlet spin-2 resonance $X^{\mu\nu}$ (for example, a Kaluza-Klein (KK) or Randall-Sundrum (RS) graviton) can be written as
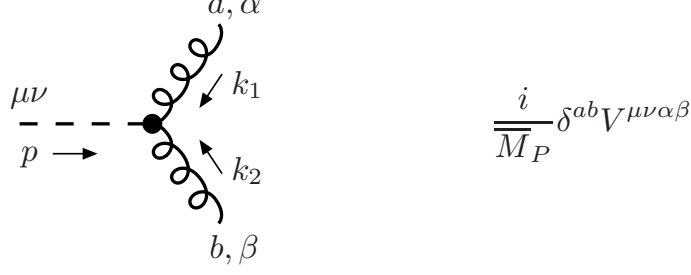
FIG. 2.4: Feynman rule for the effective coupling of spin-2 color-singlet resonance with a gluon pair, with $p^\mu + k_1^\mu + k_2^\mu = 0$. Here, $\overline{M}_P$ is a new mass scale, and $V^{\mu\nu\alpha\beta}$ is defined in eq. (2.11).

FIG. 2.5: Propagator for a massive spin-2 resonance. $D_{\mu\nu\rho\sigma}$ is defined in eq. (2.15).

[48, 107, 108]:

$$\mathcal{L} = \frac{1}{\overline{M}_P} X^{\mu\nu} \left[F^a_{\mu\rho} F^{a\rho}_\nu - \frac{1}{4} \eta_{\mu\nu} F^a_{\rho\sigma} F^{a\rho\sigma} \right], \tag{2.10}$$

where $\overline{M}_P$ is a new mass scale. The Feynman rule for the effective coupling of a massive color-singlet spin-2 particle with two gluons is shown in Figure 2.4, where

$$\begin{aligned}
V^{\mu\nu\alpha\beta} &= k_1 \cdot k_2 (\eta^{\mu\nu}\eta^{\alpha\beta} - \eta^{\mu\alpha}\eta^{\nu\beta} - \eta^{\nu\alpha}\eta^{\mu\beta}) - \eta^{\mu\nu} k_1^\beta k_2^\alpha - (k_1^\mu k_2^\nu + k_2^\mu k_1^\nu)\eta^{\alpha\beta} \\
&\quad + k_1^\mu k_2^\alpha \eta^{\nu\beta} + k_1^\nu k_2^\alpha \eta^{\mu\beta} + k_1^\beta k_2^\nu \eta^{\mu\alpha} + k_1^\beta k_2^\mu \eta^{\nu\alpha}.
\end{aligned} \tag{2.11}$$

Note this satisfies tracelessness and QCD gauge invariance conditions:

$$\eta_{\mu\nu} V^{\mu\nu\alpha\beta} = 0, \tag{2.12}$$
$$k_{1\alpha} V^{\mu\nu\alpha\beta} = 0, \tag{2.13}$$
$$k_{2\beta} V^{\mu\nu\alpha\beta} = 0. \tag{2.14}$$

One could also consider a theory where the second term (with $\eta_{\mu\nu}$) is omitted from the Lagrangian eq. (2.10). In that case, the terms containing $\eta_{\mu\nu}$ are removed from $V^{\mu\nu\alpha\beta}$, and the tracelessness condition is not satisfied. One could also consider a general linear combination of these terms. There are a few other terms that could be written down, involving higher derivatives, but they are omitted from study here.

The propagator for the massive spin-2 resonance is shown in Figure 2.5, where

$$D_{\mu\nu\rho\sigma} = \frac{1}{2} G_{\mu\rho} G_{\nu\sigma} + \frac{1}{2} G_{\mu\sigma} G_{\nu\rho} - \frac{1}{3} G_{\mu\nu} G_{\rho\sigma}, \tag{2.15}$$

$$G_{\mu\nu} = \eta_{\mu\nu} - p_\mu p_\nu / M_X^2. \tag{2.16}$$

The tensor in the numerator of the propagator can be related to a basis for the five symmetric, traceless, orthonormal external state polarization tensors for the spin-2 particle, which can be written as:

$$\epsilon^{(1)}_{\mu\nu} = \frac{1}{\sqrt{2}} \begin{pmatrix} 0 & 0 & 0 & 0 \\ 0 & 0 & 1 & 0 \\ 0 & 1 & 0 & 0 \\ 0 & 0 & 0 & 0 \end{pmatrix}, \qquad \epsilon^{(2)}_{\mu\nu} = \frac{1}{\sqrt{2}} \begin{pmatrix} 0 & 0 & 0 & 0 \\ 0 & 0 & 0 & 1 \\ 0 & 0 & 0 & 0 \\ 0 & 1 & 0 & 0 \end{pmatrix}, \qquad \epsilon^{(3)}_{\mu\nu} = \frac{1}{\sqrt{2}} \begin{pmatrix} 0 & 0 & 0 & 0 \\ 0 & 0 & 0 & 0 \\ 0 & 0 & 0 & 1 \\ 0 & 0 & 1 & 0 \end{pmatrix},$$

$$\epsilon^{(4)}_{\mu\nu} = \frac{1}{\sqrt{2}} \begin{pmatrix} 0 & 0 & 0 & 0 \\ 0 & 1 & 0 & 0 \\ 0 & 0 & -1 & 0 \\ 0 & 0 & 0 & 0 \end{pmatrix}, \qquad \epsilon^{(5)}_{\mu\nu} = \frac{1}{\sqrt{6}} \begin{pmatrix} 0 & 0 & 0 & 0 \\ 0 & 1 & 0 & 0 \\ 0 & 0 & 1 & 0 \\ 0 & 0 & 0 & -2 \end{pmatrix}. \tag{2.17}$$

These satisfy:

$$\epsilon^{(i)}_{\mu\nu} \epsilon^{(j)\mu\nu} = \delta^{ij} \qquad (i, j = 1, \ldots, 5), \tag{2.18}$$

and

$$\sum_{i=1}^{5} \epsilon^{(i)}_{\mu\nu} \epsilon^{(i)}_{\rho\sigma} = D_{\mu\nu\rho\sigma}. \tag{2.19}$$

which imply:

$$\epsilon^{(i)}_{\mu\nu} D^{\mu\nu\rho\sigma} = \epsilon^{(i)\rho\sigma} \qquad (i = 1, \ldots, 5). \tag{2.20}$$

For simplicity, we consider here only the case that the spin-2 resonance coupling to two partons is only (or mainly) to two gluons. A KK or RS graviton would also couple to $q\bar{q}$, which would result in a more complicated analysis. The interference effect would be smaller in those cases relative to the resonant dijet process, because the $q\bar{q}$ initial and final states for X production and decay of course do not interfere with the large $gg \rightarrow gg$ QCD amplitude.

We chose benchmark models as specified in Table 2.1 such that the s-channel resonant-only cross sections are close to the claimed exclusions by CMS in refs. [1, 2]. Specifically, for the resonance masses $M_X = (750, 1000, 1500, 2000, 2500, 3000)$ GeV, the observed 95% CL upper limits by CMS in refs. [1, 2] are $(5.5, 1.66, 0.42, 0.22837, 0.032155, 0.043386)$ pb. In Table 2.1, $\Gamma_{gg}^2 / \Gamma M_X$ increases as we move to higher masses, except from $M_X = 2000$ GeV to 2500 GeV; this is because the observed limit at $M_X = 2500$ GeV is evidently a downward fluctuation compared to the limits obtained at $M_X = 2000$ and 3000 GeV. For the s-channel resonant cross sections, we chose a K factor of 1.5 and an acceptance of 0.5 for the purposes

TABLE 2.1: Our choice of benchmark masses and widths for the digluon resonances in four (J=spin, color) representations considered in this paper. Here M_X, Γ, and Γ_{gg} are the mass, total width, and digluon partial width of X, respectively.

Resonance Mass	$\Gamma_{gg}^2/\Gamma M_X$			
M_X (GeV)	$J = 0$, singlet	$J = 0$, octet	$J = 1$, octet	$J = 2$, singlet
750	0.0015	0.00016	0.00005	0.0003
1000	0.002	0.0002	0.000065	0.00041
1500	0.005	0.0005	0.00015	0.001
2000	0.019	0.0018	0.00054	0.00375
2500	0.0108	0.001	0.0003	0.0022
3000	0.07	0.006	0.00183	0.014

of choosing the benchmarks. The claimed limits as a function of mass, and the predicted resonance cross-sections for an example $M_X = 2000$ GeV, are shown in Figure 2.6. For our first set of studies below, we chose the digluon partial width of X (denoted in this paper as Γ_{gg}) to be the same as the total width (Γ). More generally, if X can decay to final states that are more difficult to detect for some reason or are just not part of the dijet search (for example, $X \to jjj$ or $X \to jjjj$ or $X \to$ invisibles), then the total width Γ might exceed Γ_{gg}, and $\mathrm{BR}(X \to gg) = \Gamma_{gg}/\Gamma$.

The resonance partonic total cross-section (after angular integration, and with no cuts) in the narrow-width approximation is equal to

$$\hat{\sigma}(gg \to X \to gg) \;=\; (2j+1)k\frac{\Gamma_{gg}^2}{\Gamma M_X}\frac{\pi^2}{4}\delta(\hat{s} - M_X^2), \tag{2.21}$$

where $j = 0, 1, 2$ and $k = 1, 8$ are the spin and color of X, and $\sqrt{\hat{s}}$ is the partonic invariant mass. This can be checked as a limit in each of the special case results of the next section, and reflects the fact that there are $(2j+1)k$ times more $spin \otimes color$ states for a spin j, color k resonance than for a spin-0, color-singlet. Therefore, for our models with $j \neq 0$ and/or $k \neq 1$, we chose benchmark points that have Γ_{gg}^2/Γ approximately $(2j+1)k$ times smaller than for a spin-0, color-singlet of the same mass, in order to maintain (roughly) the same resonant total cross section.
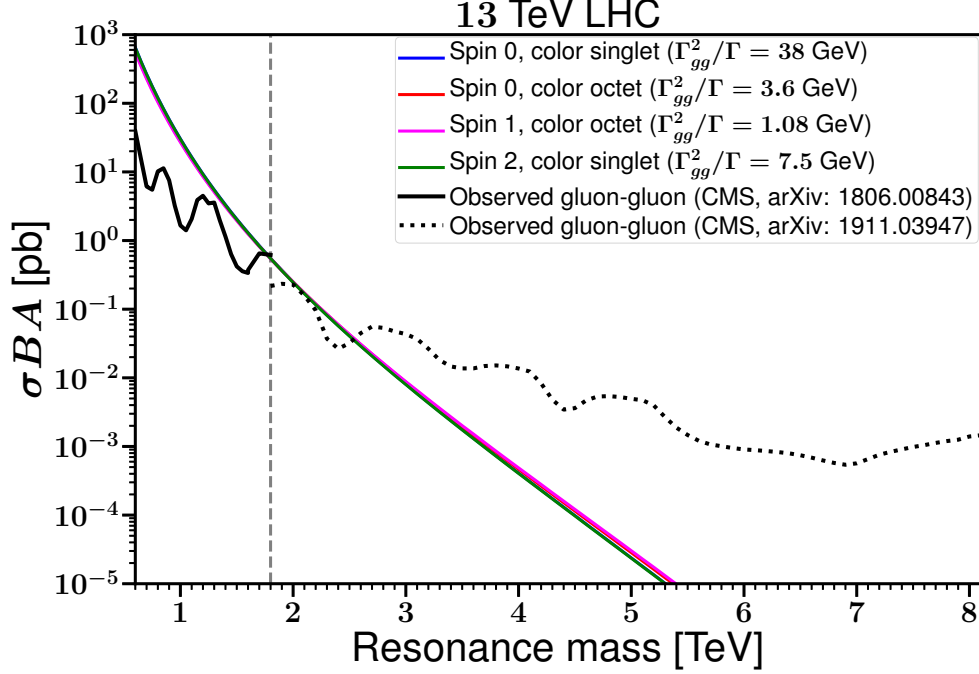
FIG. 2.6: The observed 95% CL upper limits on the product of the cross section (σ), branching fraction (B), and acceptance (A) for dijet resonances decaying to a gluon pair from ref. [2] (solid black line, left of vertical dashed gray line) and ref. [1] (dotted black line, right of vertical dashed gray line). The solid colored lines show the leading order s-channel resonant cross sections, in the narrow-width approximation, for the benchmarks for a resonance mass of 2000 GeV in each of the considered models of digluon resonances.

III. SIGNAL-BACKGROUND INTERFERENCE: PARTON-LEVEL AND MONTE CARLO METHODS

A. Parton-level approximation

For both the resonant signal $gg \to X \to gg$ and the continuum QCD background $gg \to gg$ processes, we can write an amplitude, for each choice of external gluon polarizations, in terms of a redundant basis of color combinations:

$$
\begin{aligned}
\mathcal{A}^{abcd} = \; & a_1 f^{abe} f^{cde} + a_2 f^{ace} f^{bde} + a_3 f^{ade} f^{bce} \\
& + a_4 \delta^{ab} \delta^{cd} + a_5 \delta^{ac} \delta^{bd} + a_6 \delta^{ad} \delta^{bc} \\
& + a_7 d^{abe} d^{cde} + a_8 d^{ace} d^{bde} + a_9 d^{ade} d^{bce}.
\end{aligned}
\tag{3.1}
$$

which then leads to the color sum:

$$\sum_{a,b,c,d} |\mathcal{A}^{abcd}|^2 = 72 \left(|a_1|^2 + |a_2|^2 + |a_3|^2\right) + 72 \operatorname{Re}[a_1 a_2^* - a_1 a_3^* + a_2 a_3^*]$$

$$+64 \left(|a_4|^2 + |a_5|^2 + |a_6|^2\right) + 16 \operatorname{Re}[a_4 a_5^* + a_4 a_6^* + a_5 a_6^*]$$
$$+\frac{200}{9} \left(|a_7|^2 + |a_8|^2 + |a_9|^2\right) - \frac{40}{3} \operatorname{Re}[a_7 a_8^* + a_7 a_9^* + a_8 a_9^*]$$
$$+48 \operatorname{Re}[a_1 a_5^* - a_1 a_6^* + a_2 a_4^* - a_2 a_6^* + a_3 a_4^* - a_3 a_5^*]$$
$$+40 \operatorname{Re}[a_1 a_8^* - a_1 a_9^* + a_2 a_7^* - a_2 a_9^* + a_3 a_7^* - a_3 a_8^*]$$
$$+\frac{80}{3} \operatorname{Re}[a_4 a_8^* + a_4 a_9^* + a_5 a_7^* + a_5 a_9^* + a_6 a_7^* + a_6 a_8^*]. \tag{3.2}$$

Of the nine coefficients a_i in eq. (3.1), only five are independent. This redundancy is reflected in the following QCD identities [109, 110]:

$$f^{abe} f^{cde} + f^{ace} f^{dbe} + f^{ade} f^{bce} = 0, \tag{3.3}$$

$$d^{abe} d^{cde} - \frac{1}{3} \left(f^{ace} f^{bde} + f^{ade} f^{bce}\right) = \frac{1}{3} \left(\delta^{ac} \delta^{bd} + \delta^{ad} \delta^{bc} - \delta^{ab} \delta^{cd}\right), \tag{3.4}$$

$$f^{abe} f^{cde} - d^{ace} d^{bde} + d^{bce} d^{ade} = \frac{2}{N_c} \left(\delta^{ac} \delta^{bd} - \delta^{ad} \delta^{bc}\right), \tag{3.5}$$

$$d^{abe} d^{cde} + d^{ace} d^{bde} + d^{ade} d^{bce} = \frac{1}{3} \left(\delta^{ab} \delta^{cd} + \delta^{ac} \delta^{bd} + \delta^{ad} \delta^{bc}\right). \tag{3.6}$$

where eq. (3.3) is the Jacobi identity, which holds true for the structure constants of any $SU(N_c)$ group. Eq. (3.5) also holds true for any $SU(N_c)$. On the other hand, the identities in eqs. (3.4) and (3.6) are special to $SU(3)$. It should be noted that the above four identities are not independent of each other. Namely, eq. (3.4) is obtained by using eq. (3.5) in conjunction with eq. (3.6). Also, eq. (3.4) along with eq. (3.5) gives eqs. (3.3) and (3.6). Using eqs. (3.3) and (3.4), we can eliminate the coefficients a_7, a_8, a_9, and one of a_1, a_2, or a_3 in eq. (3.1). Or we can use eqs. (3.5) and (3.6) to eliminate the coefficients a_1, a_2, a_3, and one of a_7, a_8, or a_9. In any case, we can eliminate four out of the nine coefficients a_i in eq. (3.1).

Although the QCD identities in eqs. (3.3)-(3.6) can be used to rearrange the coefficients, there are natural choices that follow from the Feynman rules. After including the contributions from t- and u-channel exchanges of X, and the interferences with QCD amplitudes, for color-singlet digluon resonances one naturally has $a_7 = a_8 = a_9 = 0$. For color-octet digluon resonances with spin 0, one has $a_4 = a_5 = a_6 = 0$. For color-octet digluon resonances with spin 1, one has $a_4 = a_5 = a_6 = a_7 = a_8 = a_9 = 0$ in eq. (3.1),

Eq. (3.2), which is understood to also include the interference terms, can then be summed over all the final states, and averaged over all the initial states for both color and spin to finally obtain the complete LO partonic differential cross section of all X exchange diagrams (signal), pure QCD background, and the interference between the signal and the background

processes. We then define:

$$\frac{d\hat{\sigma}}{dz} = \frac{d\hat{\sigma}_s}{dz} + \frac{d\hat{\sigma}_t}{dz} + \frac{d\hat{\sigma}_u}{dz} + \frac{d\hat{\sigma}_{s,t}}{dz} + \frac{d\hat{\sigma}_{t,u}}{dz} + \frac{d\hat{\sigma}_{s,u}}{dz}$$
$$+ \frac{d\hat{\sigma}_{s,QCD}}{dz} + \frac{d\hat{\sigma}_{t,QCD}}{dz} + \frac{d\hat{\sigma}_{u,QCD}}{dz}, \tag{3.7}$$

excluding the pure QCD contribution. In the above definition, $d\hat{\sigma}_{s,QCD}/dz$, for example, stands for the interference of the s-channel X exchange diagram with the pure QCD amplitude. Also, z is the cosine of the gluon scattering angle in the partonic center-of-momentum frame. Analytic formulas for all the components of $d\hat{\sigma}/dz$ as defined in eq. (3.7), for each of the digluon resonances considered, are listed next.

Spin 0, color singlet: The resonant and interference partonic cross sections at leading order for both parity-even and parity-odd spin 0, color singlets (i.e. $i = 1, 2$) are:

$$\frac{d\hat{\sigma}_s}{dz} = \frac{|c_i|^4 \hat{s}^3}{32\pi\Lambda^4 D(\hat{s})}, \tag{3.8}$$

$$\frac{d\hat{\sigma}_t}{dz} + \frac{d\hat{\sigma}_u}{dz} = \frac{|c_i|^4}{32\pi\Lambda^4 \hat{s}} \left[\frac{\hat{t}^4}{D(\hat{t})} + \frac{\hat{u}^4}{D(\hat{u})} \right], \tag{3.9}$$

$$\frac{d\hat{\sigma}_{s,t}}{dz} = \frac{|c_i|^4 \hat{s}\hat{t}^2}{256\pi\Lambda^4 D(\hat{s})D(\hat{t})} \left[(\hat{s} - M_X^2)(\hat{t} - M_X^2) + \Gamma^2 M_X^2 \right], \tag{3.10}$$

$$\frac{d\hat{\sigma}_{t,u}}{dz} = \frac{|c_i|^4 \hat{t}^2 \hat{u}^2}{256\pi\Lambda^4 \hat{s} D(\hat{t})D(\hat{u})} \left[(\hat{t} - M_X^2)(\hat{u} - M_X^2) + \Gamma^2 M_X^2 \right], \tag{3.11}$$

$$\frac{d\hat{\sigma}_{s,u}}{dz} = \frac{|c_i|^4 \hat{s}\hat{u}^2}{256\pi\Lambda^4 D(\hat{s})D(\hat{u})} \left[(\hat{s} - M_X^2)(\hat{u} - M_X^2) + \Gamma^2 M_X^2 \right], \tag{3.12}$$

$$\frac{d\hat{\sigma}_{s,QCD}}{dz} = -\frac{3\alpha_S \hat{s}}{8\Lambda^2 D(\hat{s})(1 - z^2)} \left\{ \mathrm{Re}[c_i^2](\hat{s} - M_X^2) + \mathrm{Im}[c_i^2]\Gamma M_X \right\}, \tag{3.13}$$

$$\frac{d\hat{\sigma}_{t,QCD}}{dz} = \frac{3\alpha_S \hat{s}(1 - z)^4}{256\Lambda^2 D(\hat{t})(1 + z)} \left\{ \mathrm{Re}[c_i^2](\hat{t} - M_X^2) + \mathrm{Im}[c_i^2]\Gamma M_X \right\}, \tag{3.14}$$

$$\frac{d\hat{\sigma}_{u,QCD}}{dz} = \frac{3\alpha_S \hat{s}(1 + z)^4}{256\Lambda^2 D(\hat{u})(1 - z)} \left\{ \mathrm{Re}[c_i^2](\hat{u} - M_X^2) + \mathrm{Im}[c_i^2]\Gamma M_X \right\}, \tag{3.15}$$

where $\hat{t} = \hat{s}(z - 1)/2$ and $\hat{u} = -\hat{s}(z + 1)/2$, and

$$D(\hat{s}) \equiv (\hat{s} - M_X^2)^2 + \Gamma^2 M_X^2. \tag{3.16}$$

Also, the LO partial width into the digluon final state is

$$\Gamma_{gg} = \frac{|c_i|^2 M_X^3}{2\pi\Lambda^2}. \tag{3.17}$$

Spin 0, color octet: The resonant and interference partonic cross sections at leading order for both scalar and pseudo-scalar color octets (i.e. $i = 3, 4$) are:

$$\frac{d\hat{\sigma}_{\rm s}}{dz} = \frac{25|c_i|^4\hat{s}^3}{2304\pi\Lambda^4 D(\hat{s})}, \tag{3.18}$$

$$\frac{d\hat{\sigma}_{\rm t}}{dz} + \frac{d\hat{\sigma}_{\rm u}}{dz} = \frac{25|c_i|^4}{2304\pi\Lambda^4\hat{s}}\left[\frac{\hat{t}^4}{D(\hat{t})} + \frac{\hat{u}^4}{D(\hat{u})}\right], \tag{3.19}$$

$$\frac{d\hat{\sigma}_{\rm s,t}}{dz} = -\frac{5|c_i|^4\hat{s}\hat{t}^2}{1536\pi\Lambda^4 D(\hat{s})D(\hat{t})}\left[(\hat{s} - M_X^2)(\hat{t} - M_X^2) + \Gamma^2 M_X^2\right], \tag{3.20}$$

$$\frac{d\hat{\sigma}_{\rm t,u}}{dz} = -\frac{5|c_i|^4\hat{t}^2\hat{u}^2}{1536\pi\Lambda^4\hat{s}D(\hat{t})D(\hat{u})}\left[(\hat{t} - M_X^2)(\hat{u} - M_X^2) + \Gamma^2 M_X^2\right], \tag{3.21}$$

$$\frac{d\hat{\sigma}_{\rm s,u}}{dz} = -\frac{5|c_i|^4\hat{s}\hat{u}^2}{1536\pi\Lambda^4 D(\hat{s})D(\hat{u})}\left[(\hat{s} - M_X^2)(\hat{u} - M_X^2) + \Gamma^2 M_X^2\right], \tag{3.22}$$

$$\frac{d\hat{\sigma}_{\rm s,QCD}}{dz} = -\frac{5\alpha_S\hat{s}}{16\Lambda^2 D(\hat{s})(1 - z^2)}\left\{{\rm Re}[c_i^2](\hat{s} - M_X^2) + {\rm Im}[c_i^2]\Gamma M_X\right\}, \tag{3.23}$$

$$\frac{d\hat{\sigma}_{\rm t,QCD}}{dz} = \frac{5\alpha_S\hat{s}(1 - z)^4}{512\Lambda^2 D(\hat{t})(1 + z)}\left\{{\rm Re}[c_i^2](\hat{t} - M_X^2) + {\rm Im}[c_i^2]\Gamma M_X\right\}, \tag{3.24}$$

$$\frac{d\hat{\sigma}_{\rm u,QCD}}{dz} = \frac{5\alpha_S\hat{s}(1 + z)^4}{512\Lambda^2 D(\hat{u})(1 - z)}\left\{{\rm Re}[c_i^2](\hat{u} - M_X^2) + {\rm Im}[c_i^2]\Gamma M_X\right\}, \tag{3.25}$$

and the partial width into the digluon final state is

$$\Gamma_{gg} = \frac{5|c_i|^2 M_X^3}{48\pi\Lambda^2}. \tag{3.26}$$

In the case that the decay width is entirely due to digluons, we can compare the s-channel resonant production cross-section to that of the spin-0, color-singlet case, using

$$\frac{1}{D(\hat{s})} = \frac{\pi}{\Gamma M_X}\delta(\hat{s} - M_X^2). \tag{3.27}$$

This means that the s-channel resonant cross-sections can be written as

$$\frac{d\hat{\sigma}_s}{dz} = n_i^s\frac{\pi|c_i|^2 M_X^2}{\Lambda^2}\delta(\hat{s} - M_X^2), \tag{3.28}$$

where for spin 0, color singlets,

$$n_1^s = n_2^s = 1/16, \tag{3.29}$$

and for spin 0, color octets,

$$n_3^s = n_4^s = 5/48. \tag{3.30}$$

To have the same resonant cross-section, we could take $|c_3|^2 = (3/5)|c_1|^2$. In that case, comparing eqs. (3.13)-(3.15) and (3.23)-(3.25), we see that the pre-factor for the interference cross-section would be half as big for the color-octet case as for the color-singlet case. So, all other things being equal, the importance of the interference terms relative to the resonance terms is half as big in the color-octet spin-0 case as in the color-singlet spin-0 case.

Spin 1, color octet: The resonant and interference partonic cross sections at leading order for a spin-1, color-octet resonance are:

$$\frac{d\hat{\sigma}_s}{dz} = \frac{9|c_5|^4 \hat{s}^5 z^2}{256\pi\Lambda^8 D(\hat{s})}, \tag{3.31}$$

$$\frac{d\hat{\sigma}_t}{dz} + \frac{d\hat{\sigma}_u}{dz} = \frac{9|c_5|^4 \hat{s}}{1024\pi\Lambda^8}\left[\frac{\hat{t}^4(3+z)^2}{D(\hat{t})} + \frac{\hat{u}^4(3-z)^2}{D(\hat{u})}\right], \tag{3.32}$$

$$\frac{d\hat{\sigma}_{s,t}}{dz} = \frac{9|c_5|^4 \hat{s}^3 \hat{t}^2 z(3+z)}{1024\pi\Lambda^8 D(\hat{s})D(\hat{t})}\left[(\hat{s} - M_X^2)(\hat{t} - M_X^2) + \Gamma^2 M_X^2\right], \tag{3.33}$$

$$\frac{d\hat{\sigma}_{t,u}}{dz} = \frac{9|c_5|^4 \hat{s}\hat{t}^2\hat{u}^2(9-z^2)}{2048\pi\Lambda^8 D(\hat{t})D(\hat{u})}\left[(\hat{t} - M_X^2)(\hat{u} - M_X^2) + \Gamma^2 M_X^2\right], \tag{3.34}$$

$$\frac{d\hat{\sigma}_{s,u}}{dz} = -\frac{9|c_5|^4 \hat{s}^3 \hat{u}^2 z(3-z)}{1024\pi\Lambda^8 D(\hat{s})D(\hat{u})}\left[(\hat{s} - M_X^2)(\hat{u} - M_X^2) + \Gamma^2 M_X^2\right], \tag{3.35}$$

$$\frac{d\hat{\sigma}_{s,\text{QCD}}}{dz} = -\frac{9\alpha_S \hat{s}^2 z^2}{16\Lambda^4 D(\hat{s})(1-z^2)}\left\{\text{Re}[c_5^2](\hat{s} - M_X^2) + \text{Im}[c_5^2]\Gamma M_X\right\}, \tag{3.36}$$

$$\frac{d\hat{\sigma}_{t,\text{QCD}}}{dz} = -\frac{9\alpha_S \hat{s}^2(3+z)^2(1-z)^3}{1024\Lambda^4 D(\hat{t})(1+z)}\left\{\text{Re}[c_5^2](\hat{t} - M_X^2) + \text{Im}[c_5^2]\Gamma M_X\right\}, \tag{3.37}$$

$$\frac{d\hat{\sigma}_{u,\text{QCD}}}{dz} = -\frac{9\alpha_S \hat{s}^2(3-z)^2(1+z)^3}{1024\Lambda^4 D(\hat{u})(1-z)}\left\{\text{Re}[c_5^2](\hat{u} - M_X^2) + \text{Im}[c_5^2]\Gamma M_X\right\}, \tag{3.38}$$

and the partial width into the digluon final state is

$$\Gamma_{gg} = \frac{|c_5|^2 M_X^5}{16\pi\Lambda^4}. \tag{3.39}$$

Spin 2, color singlet: The resonant and interference partonic cross sections at leading order for a spin-2, color-singlet resonance are:

$$\frac{d\hat{\sigma}_s}{dz} = \frac{\hat{s}^3(1+6z^2+z^4)}{512\pi\overline{M}_P^4 D(\hat{s})}, \tag{3.40}$$

$$\frac{d\hat{\sigma}_t}{dz} = \frac{\hat{s}^3(17+4z+6z^2+4z^3+z^4)}{1024\pi\overline{M}_P^4 D(\hat{t})}, \tag{3.41}$$

$$\frac{d\hat{\sigma}_{\text{u}}}{dz} = \frac{\hat{s}^3(17 - 4z + 6z^2 - 4z^3 + z^4)}{1024\pi\overline{M}_P^4 D(\hat{u})}, \tag{3.42}$$

$$\frac{d\hat{\sigma}_{\text{s,t}}}{dz} = \frac{\hat{s}^3(1 + z)^4}{4096\pi\overline{M}_P^4 D(\hat{s})D(\hat{t})} \left[(\hat{s} - M_X^2)(\hat{t} - M_X^2) + \Gamma^2 M_X^2\right], \tag{3.43}$$

$$\frac{d\hat{\sigma}_{\text{t,u}}}{dz} = \frac{\hat{s}^3}{256\pi\overline{M}_P^4 D(\hat{t})D(\hat{u})} \left[(\hat{t} - M_X^2)(\hat{u} - M_X^2) + \Gamma^2 M_X^2\right], \tag{3.44}$$

$$\frac{d\hat{\sigma}_{\text{s,u}}}{dz} = \frac{\hat{s}^3(1 - z)^4}{4096\pi\overline{M}_P^4 D(\hat{s})D(\hat{u})} \left[(\hat{s} - M_X^2)(\hat{u} - M_X^2) + \Gamma^2 M_X^2\right], \tag{3.45}$$

$$\frac{d\hat{\sigma}_{\text{s,QCD}}}{dz} = -\frac{3\alpha_S\hat{s}(\hat{s} - M_X^2)(1 + 6z^2 + z^4)}{64\overline{M}_P^2 D(\hat{s})(1 - z^2)}, \tag{3.46}$$

$$\frac{d\hat{\sigma}_{\text{t,QCD}}}{dz} = \frac{3\alpha_S\hat{s}(\hat{t} - M_X^2)(17 + 4z + 6z^2 + 4z^3 + z^4)}{256\overline{M}_P^2 D(\hat{t})(1 - z^2)}, \tag{3.47}$$

$$\frac{d\hat{\sigma}_{\text{u,QCD}}}{dz} = \frac{3\alpha_S\hat{s}(\hat{u} - M_X^2)(17 - 4z + 6z^2 - 4z^3 + z^4)}{256\overline{M}_P^2 D(\hat{u})(1 - z^2)}. \tag{3.48}$$

The pure X-exchange parts and their corresponding interference-with-QCD terms have common angular factors of $(1 + 6z^2 + z^4)$, $(17 + 4z + 6z^2 + 4z^3 + z^4)$, and $(17 - 4z + 6z^2 - 4z^3 + z^4)$ for s-, t-, and u-channels respectively.

The digluon partial width of the resonance is

$$\Gamma_{gg} = \frac{M_X^3}{10\pi\overline{M}_P^2}. \tag{3.49}$$

In the narrow width approximation of eq. (3.27), assuming that X has no other decays, we therefore have

$$\frac{d\hat{\sigma}_s}{dz} = \frac{5\pi M_X^2}{256\overline{M}_P^2}(1 + 6z^2 + z^4)\delta(\hat{s} - M_X^2). \tag{3.50}$$

Having obtained the analytic formulas for all the components of $d\hat{\sigma}/dz$, for all four models considered, we can then compute the LO digluon production cross section at the LHC,

$$\frac{d\sigma_{pp \to gg}}{d(\sqrt{\hat{s}})} = \sqrt{\hat{s}} \int_{x_-}^{x_+} \frac{dx}{xs} g(x)g\left(\frac{\hat{s}}{xs}\right) \int_{-z_{\text{cut}}}^{z_{\text{cut}}} dz \frac{d\hat{\sigma}}{dz}. \tag{3.51}$$

Here, x is the longitudinal momentum fraction for the parton, $g(x)$ is the gluon parton distribution function (PDF) obtained from the NNPDF2.3 LO PDF set [111] with factorization scale $\mu_F = M_X$, $\sqrt{s}$ is the total energy of the pp collisions at the LHC, and $\sqrt{\hat{s}}$ is the invariant mass of the gluon pairs in both initial and final states. In eq. (3.51), we have

imposed cuts on the transverse momentum and the pseudo-rapidity of the gluons:

$$p_{T_j} > p_{T_j}^{\mathrm{cut}} = 100 \text{ GeV}, \tag{3.52}$$

$$|\eta_j| < \eta_j^{\mathrm{cut}} = 2.5, \tag{3.53}$$

respectively. Also, in order to increase the significance of resonance signal, CMS has defined signal regions that cut on the difference between the pseudo-rapidities of the two jets:

$$\Delta\eta = |\eta_{j_1} - \eta_{j_2}| < (\Delta\eta)^{\mathrm{cut}}. \tag{3.54}$$

We will follow CMS by choosing $(\Delta\eta)^{\mathrm{cut}} = 1.1$ for $M_X > 1800$ GeV as in [2], and $(\Delta\eta)^{\mathrm{cut}} = 1.3$ for $M_X < 1800$ GeV as in [1]. For a parton level analysis, these cuts can be imposed by using

$$x_\pm = e^{\pm\eta_j^{\mathrm{cut}}}\sqrt{\hat{s}/s}, \tag{3.55}$$

$$z_{\mathrm{cut}} = \mathrm{Min}\left[\sqrt{1 - 4p_{T_j}^{\mathrm{cut}\,2}/\hat{s}}, \ \tanh\left(\eta_j^{\mathrm{cut}} - \frac{1}{2}\left|\ln\left(x^2 s/\hat{s}\right)\right|\right), \ \tanh\left((\Delta\eta)^{\mathrm{cut}}/2\right)\right] \tag{3.56}$$

in eq. (3.51).

Then to obtain more realistic distributions roughly approximating the experimental ones, the parton-level distributions of $d\sigma_{pp\to gg}/d(\sqrt{\hat{s}})$ in eq. (3.51) can be smeared by convolution with an approximate detector response dijet mass distribution, shown for the case of a digluon invariant mass $m_{gg} = (1000, 2000, 3000)$ GeV in Figure 3.1. To obtain the approximate detector responses for the dijet invariant mass distributions, we used a sample of detector-level events, generated with PYTHIA 8.2 [112, 113] and DELPHES 3.4 [114], obtained from (at least 1.5×10^7) parton-level events for the resonant process $gg \to X \to gg$ with the required digluon invariant mass, here $\sqrt{\hat{s}} = m_{gg} = 1000$, 2000, and 3000 GeV, using the same cuts and procedure for combining jets into wide jets as described in the next subsection. This was done for each of the four (spin, color) quantum number combinations described above.

The results obtained by the above simple procedure will be referred to below as the parton-level approximation (with smearing). This method can be viewed as a quick approximation and qualitative independent cross-check of the more involved method we describe next, which is much more demanding of computer resources.

B. Showering, hadronization, and detector-level simulation

For a much more realistic approximation, referred to below simply as the detector-level simulation, we used MADGRAPH5_AMC@NLO v2.6.6 [115] for all our LO event simulations, which uses a *Universal FeynRules Output (UFO)* file generated by FEYNRULES v2.3 [116], a MATHEMATICA package to get the Feynman rules from an input Lagrangian. We
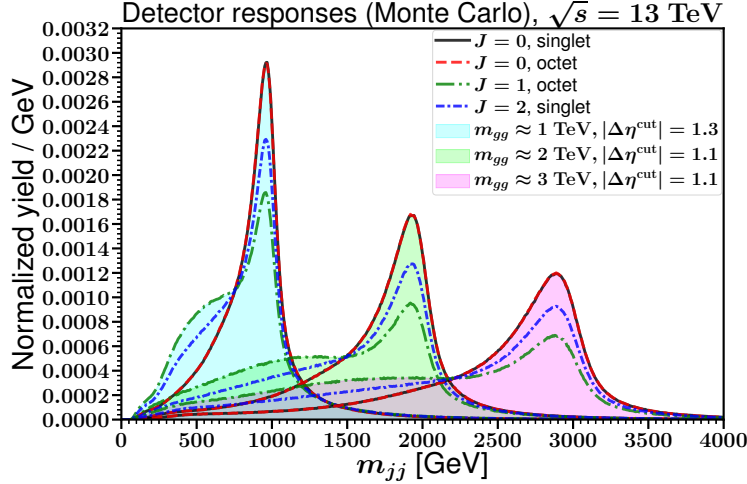
FIG. 3.1: The normalized detector response dijet mass distributions for two wide jets, for digluon masses m_{gg} = 1000, 2000, and 3000 GeV and various spin and color quantum numbers, generated and analyzed using PYTHIA 8 and DELPHES.

used PYTHIA 8.2 for showering and hadronization, and DELPHES 3.4 for detector simulation.

Using MADGRAPH, our goal was not only to generate detector-level events for the signal, including all X exchange diagrams, but also for the interference between the signal and the QCD background $gg \to gg$. One of the the challenges to generate detector-level events for the interference terms is that some of the generated events have negative cross-sections. (Simply generating a full QCD+X sample and then subtracting the pure QCD part is not practical, because of the very poor statistics. The actual LHC experiment has much better statistics than our simulations can provide.) In order to keep track of the events with positive and negative cross-sections, the parton-level events for the interference terms are divided into two sets, one with positive cross-sections, and the other with negative cross-sections. The detector-level events for both sets are independently obtained. Then, to obtain the dijet invariant mass distributions for the interference terms, the distributions with negative cross-section events are subtracted bin-by-bin from the ones with positive cross-section events.

Another problem is that MADGRAPH cannot assign a unique color flow [117–119] for each parton-level event for the interference between the QCD background $gg \to gg$ and color-singlet resonant signal $gg \to X \to gg$, thus disabling PYTHIA from showering and hadronization, thereby precluding the generation of any detector-level events. To get around this, we independently generated detector-level events for the interference between the QCD background and the color-singlet resonant signal by simply assigning a color flow by fiat to each event. There are four physically distinct color-flow possibilities, as shown in Fig. 3.2. We therefore repeated the analysis four times, each time with the same color flow assigned to every event. Thus, for color-singlet resonances, we obtain a spread of the possible differential cross sections by taking the maximum and minimum of the four possibilities in each invariant mass bin, as will be shown below in Figs. 4.2, 4.8, 5.2, and 5.8. On the other hand, this problem does not occur for color-octet resonances, as they are uniquely determined to have the same color charge as that of a gluon.

We generated at least 5×10^6 events for both the digluon resonant signal and the interference between the signal and the QCD background, for pp collisions at $\sqrt{s} = 13$ TeV, for each of the considered digluon resonant benchmark mass models. While generating events with
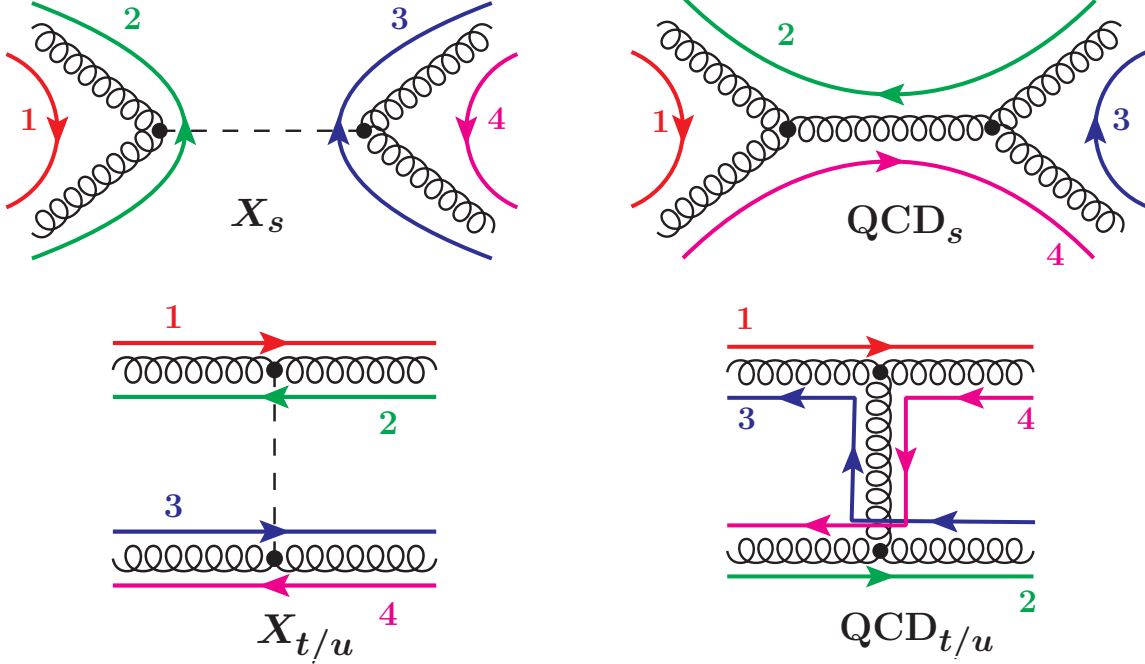
FIG. 3.2: The four distinct color flows for the parton-level events for the interference between the color-singlet digluon resonant process $gg \to X \to gg$ and the QCD process $gg \to gg$. These color flows are referred to below in the text as X_s, $X_{t/u}$, QCD_s, and $\text{QCD}_{t/u}$, as labeled. The integer tags (e.g. 1-4) for the color flow lines are required by the showering and hadronization event generators to begin the parton shower. For example, in PYTHIA, the integer tags are typically assigned as 501-504.

MADGRAPH, we used MADGRAPH's default parton distribution functions (PDFs) based on NNPDF2.3 LO set [111] with factorization and renormalization scales $\mu_F = \mu_R = M_X$.

In our analysis, all the jets are required to satisfy a cut on pseudo-rapidity $|\eta_j| < 2.5$ as noted above in eq. (3.53). To obtain the dijet mass (m_{jj}), we follow the procedure used by CMS in refs. [1, 2] to reduce the sensitivity to radiation of additional gluons from the final-state gluons in the hard-scattering event. Specifically, we start with the two leading p_T jets, and the four-vectors of all other jets within $\Delta R = \sqrt{(\Delta\eta)^2 + (\Delta\phi)^2} < 1.2$ of the two leading p_T jets are added to the nearest leading jet to obtain two wide jets. These wide jets are then required to satisfy the cut $p_{T_j} > p_{T_j}^{\text{wide-jets}} = 100$ GeV, as noted above in eq. (3.52). Finally, as also already mentioned in the previous section, we follow CMS by defining the signal region to have a cut on the difference in pseudo-rapidity for the two wide jets, $|\Delta\eta_{jj}| < 1.3$ (for resonance masses smaller than 1.8 TeV as in [1]), and $|\Delta\eta_{jj}| < 1.1$ (for resonance masses larger than 1.8 TeV as in [2]). This preferentially eliminates the pure background events, and tends to improve the efficiency for pure resonance events compared to interference. However, as we will see it certainly does not reduce the effects of interference to a negligible level.

IV.   RESULTS FOR $\Gamma = \Gamma_{gg}$

In this section, we show results obtained for our benchmark model cases. In each case, we start with results obtained using the simple method of parton-level generation with smearing as outlined in subsection III A. These are followed by results for the full detector simulation of subsection III B. In this section, we consider the case $\Gamma_{gg} = \Gamma$, for which the relative effects of the interference are minimized.

A.   Spin 0, color singlet

1.   Parton-level with smearing

The left panels of Figure 4.1 show the leading order digluon invariant mass distributions, obtained by parton-level leading order calculation, for pp collisions at $\sqrt{s} = 13$ TeV, for a spin-0, color-singlet resonance, for benchmark examples from Table 2.1 with resonance masses of 1000, 2000, and 3000 GeV in the top, middle and bottom rows, respectively. We remind that the chosen benchmark values of $\Gamma_{gg} = \Gamma$ predict a resonant-only cross-section about equal to the current CMS limit from ref. [2]. The parton-level distributions are in the left column, and the right column shows the results after smearing by convolution with approximate detector responses (as shown in Figure 3.1), to obtain a rough estimate of dijet mass distributions. In all six panels, the red lines show the naive results for the resonant signal $gg \to X \to gg$ with all X exchange diagrams, while the blue lines show the full results including the interferences with the QCD background $gg \to gg$. (The pure QCD background contribution is much larger and is not shown, here or in the following.)

From Figure 4.1, we see that when interferences with QCD amplitudes are included, the dijet mass distributions (blue lines) are both qualitatively and quantitatively different from that of distributions with only the X exchange diagrams (red lines). In the parton-level results in the left column panels, with interference included, we see a peak below and a dip above the resonance mass rather than just a resonance peak. The origin of the peak/dip signature can be traced back to the term $\hat{s} - M_X^2$ in $d\hat{\sigma}_{s,\mathrm{QCD}}/dz$, as given in eq. (3.13). The magnitude of the interference is, in general, enhanced for $\sqrt{\hat{s}}$ below M_X because of the steeply falling gluon PDFs. After smearing (right column panels), the dip at higher invariant masses manifests as a deficit of events compared to the naive resonance results. For the results with interference included, we can also note that the peak below the resonance mass is significantly larger than the naive resonance peak that we get from not including the interference terms. However, the larger peak is counteracted by the fact that it is connected to a large low-energy tail. If the low-energy tail is absorbed into a QCD background fit (which we do not attempt in this paper, and can probably be done in a variety of distinct ways), an effective dip for $m_{jj} > M_X$ would probably result. We have checked that the interference effect would have been larger without the imposition of the $\Delta \eta$ cut. Correctly deriving a limit on these distribution shapes as new physics sources might require a more flexible analysis strategy than just modeling a resonance peak, even if the pure resonance contribution is very narrow compared to the experimental resolution.

As the experimental data sets are increased in the future, so that one is probing models with even smaller cross-sections, we have checked that the relative importance of the interference and the pure resonance at a given M_X stays nearly constant. We have also checked that this feature holds true for the other digluon resonances considered in this paper. On the other hand, as the mass is increased, Figure 4.1 shows that the relative importance of the interference tends to increase substantially, particularly in the low-mass tail.

2. Monte Carlo results with showering, hadronization, and detector simulation

In Figure 4.2, we show the dijet invariant mass distributions for the considered benchmarks of Table 2.1 with $\Gamma = \Gamma_{gg}$, at 13 TeV LHC, for spin-0, color-singlet resonances, this time obtained using Monte Carlo generation of events followed by simulations with showering, hadronization and detector simulation.[†] The results are shown for a digluon resonant process $gg \rightarrow X \rightarrow gg$, which include only the s-, t-, and u-channel exchanges of X (red line), and the full results. Here, the shaded blue region is the envelope of the results for the four possible color flows, as discussed above in reference to Figure 3.2.

From Figure 4.2, we note that the impact of QCD interference is least if we assume the color flow is always the one that we have labeled X_s (corresponding to the s-channel resonant process), and is greatest if we instead assume either the $X_{t/u}$ and $QCD_{t/u}$ color flows, which produce almost identical results. The color flow labeled QCD_s produces intermediate results. In any case, the QCD interference again is seen to change the naively expected resonance peak shape in a way consistent with the previous discussion. Again, we note that the relative importance of interference seems to increase with the resonance mass. The right-hand panels of Figure 4.2 can be compared to the right-hand panels of Figure 4.1, as both have the same masses $M_X = 1000, 2000, 3000$ GeV. The match is of course not an exact one, because the smearing method using the detector responses in Figure 3.1, is only a very rough approximation to the full-fledged event generation with showering, hadronization and detector simulation, and furthermore the color-flow uncertainty is evidently a non-trivial one. The more complete treatment tends to give lower yields in this case. However, the qualitative similarity between the results of the two methods is a useful check. Even the more complete detector simulation is of course different from the true CMS and ATLAS detector responses.

[†] As a check of our implementation of the X interactions using FEYNRULES, we verified that the parton-level distributions obtained using MADGRAPH (not shown here) closely match the parton-level distributions obtained by our calculations as described in Section III A and shown in Figure 4.1. A similar check was done for each of the other (spin, color) combinations for X.
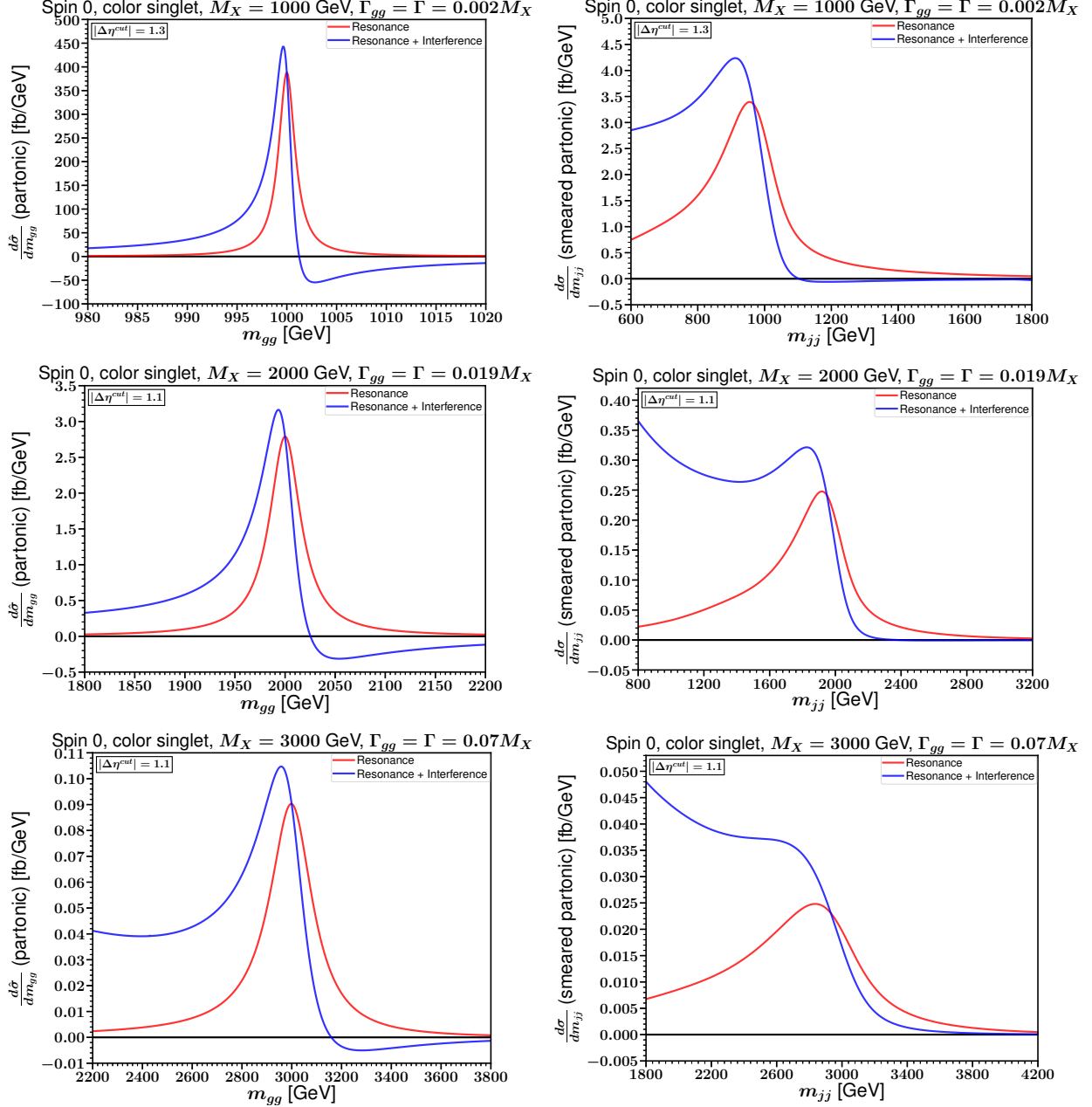
FIG. 4.1: Digluon invariant mass distributions, at the 13 TeV LHC, for spin-0, color-singlet resonances with $(M_X, \Gamma/M_X) = (1000 \text{ GeV}, 0.002)$ [top row] and $(2000 \text{ GeV}, 0.019)$ [middle row] and $(3000 \text{ GeV}, 0.07)$ [bottom row]. The parton-level distributions are shown in the left column panels. These are are then smeared by convolution with the estimated detector responses shown in Figure 3.1 to obtain the dijet invariant mass distributions in the panels of the right columns. In all six panels, the red lines show the naive results for the resonant signal $gg \to X \to gg$, while the blue lines show the full results including the interferences with the QCD background $gg \to gg$.
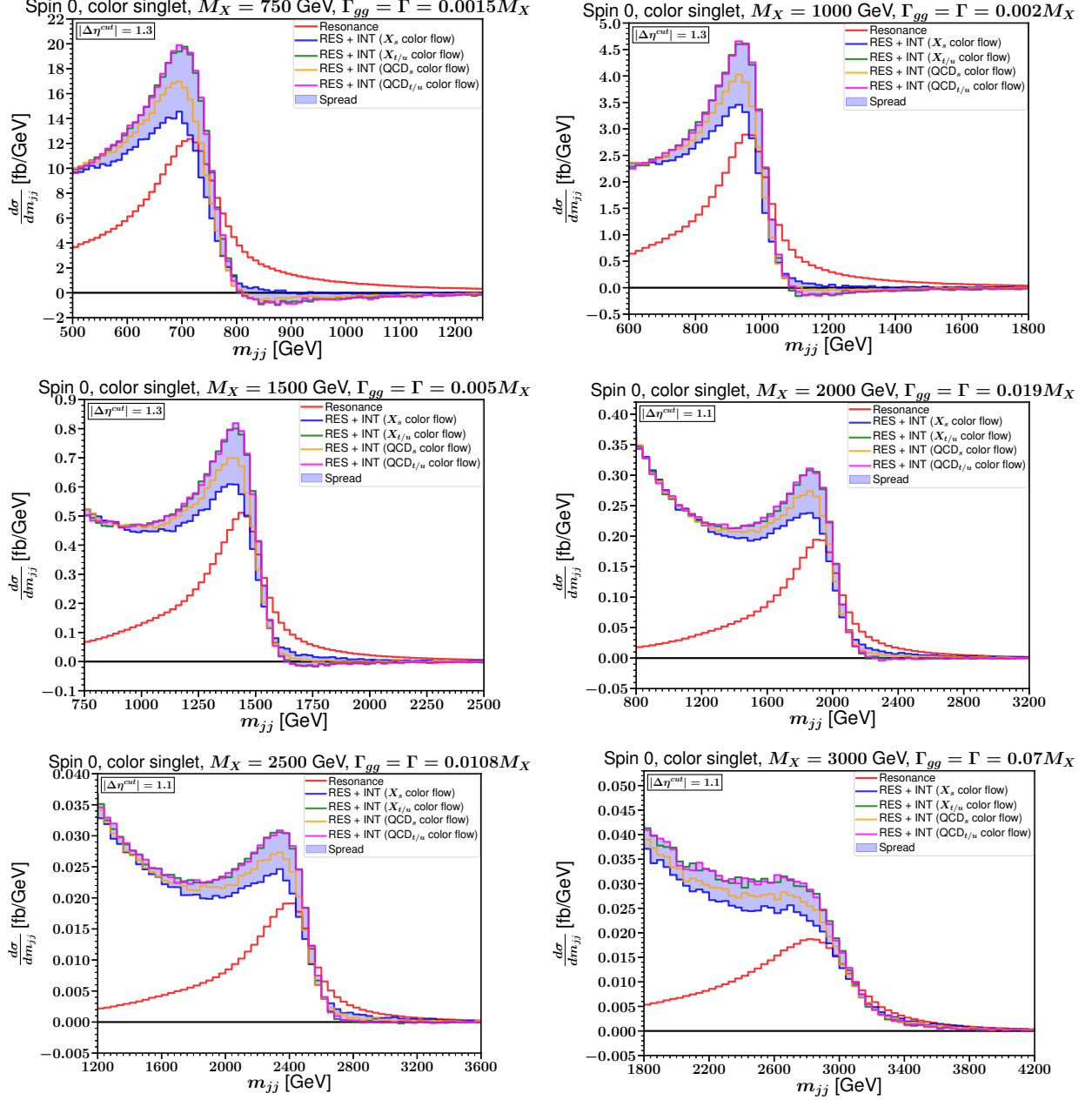
FIG. 4.2: Dijet invariant mass distributions for the spin-0, color-singlet benchmarks of Table 2.1 with $\Gamma = \Gamma_{gg}$, at the 13 TeV LHC, obtained with showering, hadronization and detector simulation. The red lines show the naive results with only the resonance diagrams of $gg \to X \to gg$ process (RES), which include the s-, t-, and u-channel exchanges of X, while the other four colored lines show the full results including interferences with the continuum QCD $gg \to gg$ amplitudes (INT) for all four color flows shown in Figure 3.2, as labeled. The shaded region shows the spread in the full result in each invariant mass bin for different color flow choices. The cases shown in the right column can be compared directly to those in the right column of the previous Figure 4.1 based on the more simplistic method of parton level with smearing.

B.   Spin 0, color octet

1.   Parton-level with smearing

In Figure 4.3, we show the parton-level digluon invariant mass distributions for pp collisions at $\sqrt{s} = 13$ TeV, for massive spin-0, color-octet resonances, for the benchmark examples of Table 2.1 with masses 1000, 2000, and 3000 GeV in the top, middle and bottom rows, respectively. As in the previous subsection, the parton-level distributions before smearing are shown in the left panels, and the right panels show the distributions after convolution with approximate detector responses shown in Figure 3.1, as described in Section III A. In all six panels, the red lines show the results for the resonant signal $gg \to X \to gg$ with all X exchange diagrams, while the blue lines show the full results including the interferences with the QCD amplitudes $gg \to gg$.

Just as was the case for spin-0, color-singlet resonances, the parton-level results before smearing show a peak below $m_{jj} < M_X$ and a dip above $m_{jj} > M_X$ for the full result (blue line), as opposed to a pure peak (red line) that we get without including the interference terms. After smearing, the deficit above the input resonance mass, compared to the naive result, does not appear as considerable as in the color-singlet case. The main feature is again the presence of the low-mass positive tail. Depending on how this would be absorbed into the QCD background fit, this could again lead to both a peak slightly below M_X and an apparent dip in the differential distribution above M_X. However, the interference effects for spin-0, color-octet resonances are not as big as for spin-0, color-singlets, as we anticipated above in the discussion immediately following eq. (3.30).

2.   Monte Carlo results with showering, hadronization, and detector simulation

Figure 4.4 shows the dijet invariant mass distributions for the considered benchmarks of Table 2.1 with X assumed to always decay to a pair of gluons, at 13 TeV LHC, for spin-0, color-octet resonances, obtained using Monte Carlo simulations. The results are shown for the naive resonant process $gg \to X \to gg$, and for the full results, which also include the interferences with the continuum QCD $gg \to gg$ amplitudes.

From Figure 4.4, the QCD interference with a spin-0, color-octet resonance has the aforementioned feature of having less dramatic positive tails in the region $m_{jj} < M_X$ with almost no negative tails in the region $m_{jj} > M_X$. Unlike the case of a color-singlet scalar, here we have exactly one result for the QCD interferences because the color flow is uniquely determined. The relative importance of the interference again increases as one moves to higher resonance masses M_X. Again, comparing the right column panels of Figure 4.4 to the corresponding right column panels of Figure 4.3, which have the same masses 1000, 2000, and 3000 GeV, the fully simulated results don't exactly match with the smeared parton-level results, with the more complete simulation producing a lower yield, but the shapes are reassuringly qualitatively similar.
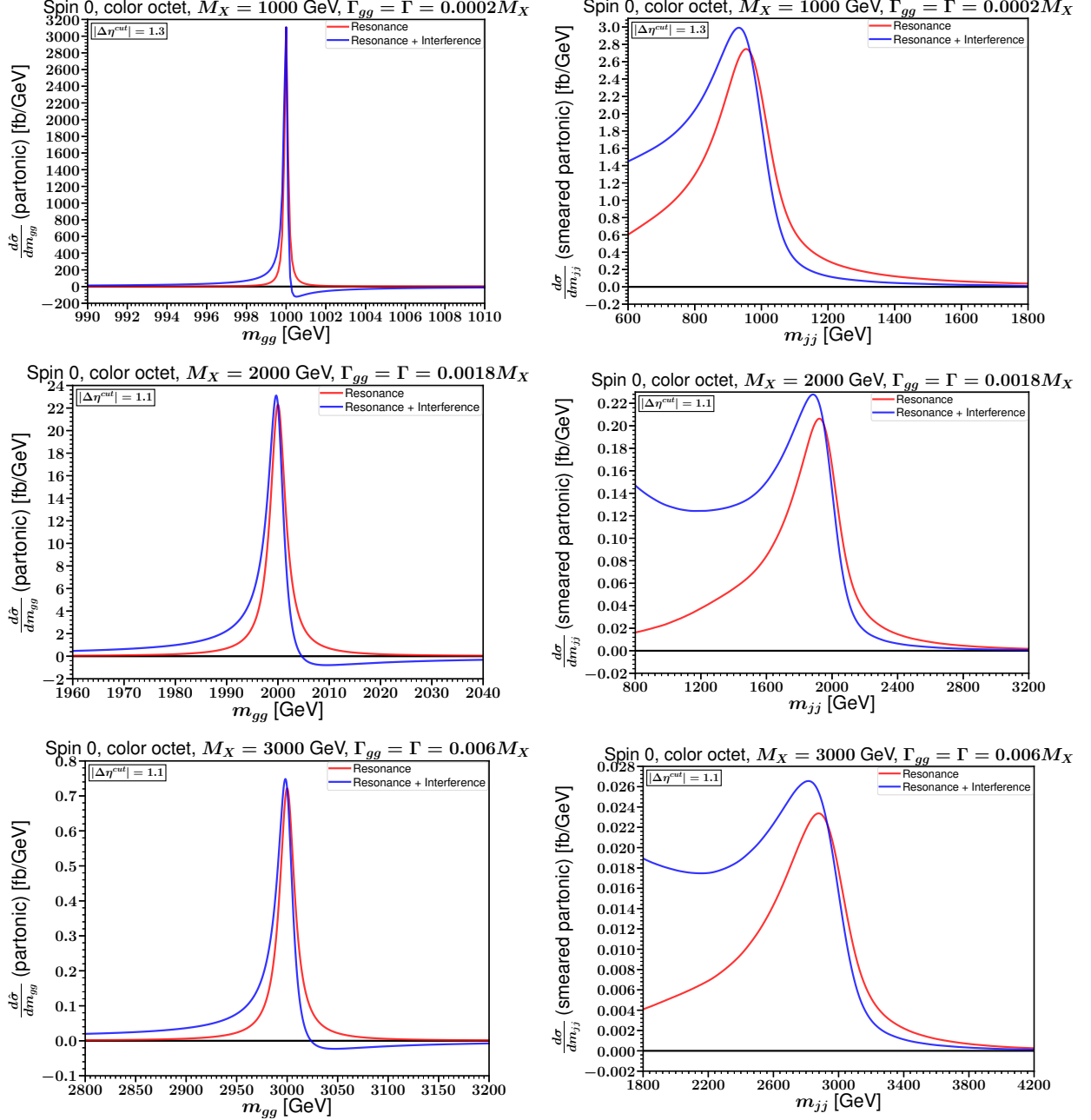
FIG. 4.3: Digluon invariant mass distributions, at the 13 TeV LHC, for spin-0, color-octet resonances with $(M_X, \Gamma/M_X) = (1000 \text{ GeV}, 0.0002)$ [top row], $(2000 \text{ GeV}, 0.0018)$ [middle row], and $(3000 \text{ GeV}, 0.006)$ [bottom row]. The parton-level distributions are shown in the left column panels. These are then smeared by convolution with the detector responses shown in Figure 3.1, to obtain the dijet invariant mass distributions in the right panels. In all six panels, the red lines show the naive results for the resonant signal $gg \to X \to gg$, while the blue lines show the full results including the interferences with the QCD background $gg \to gg$.
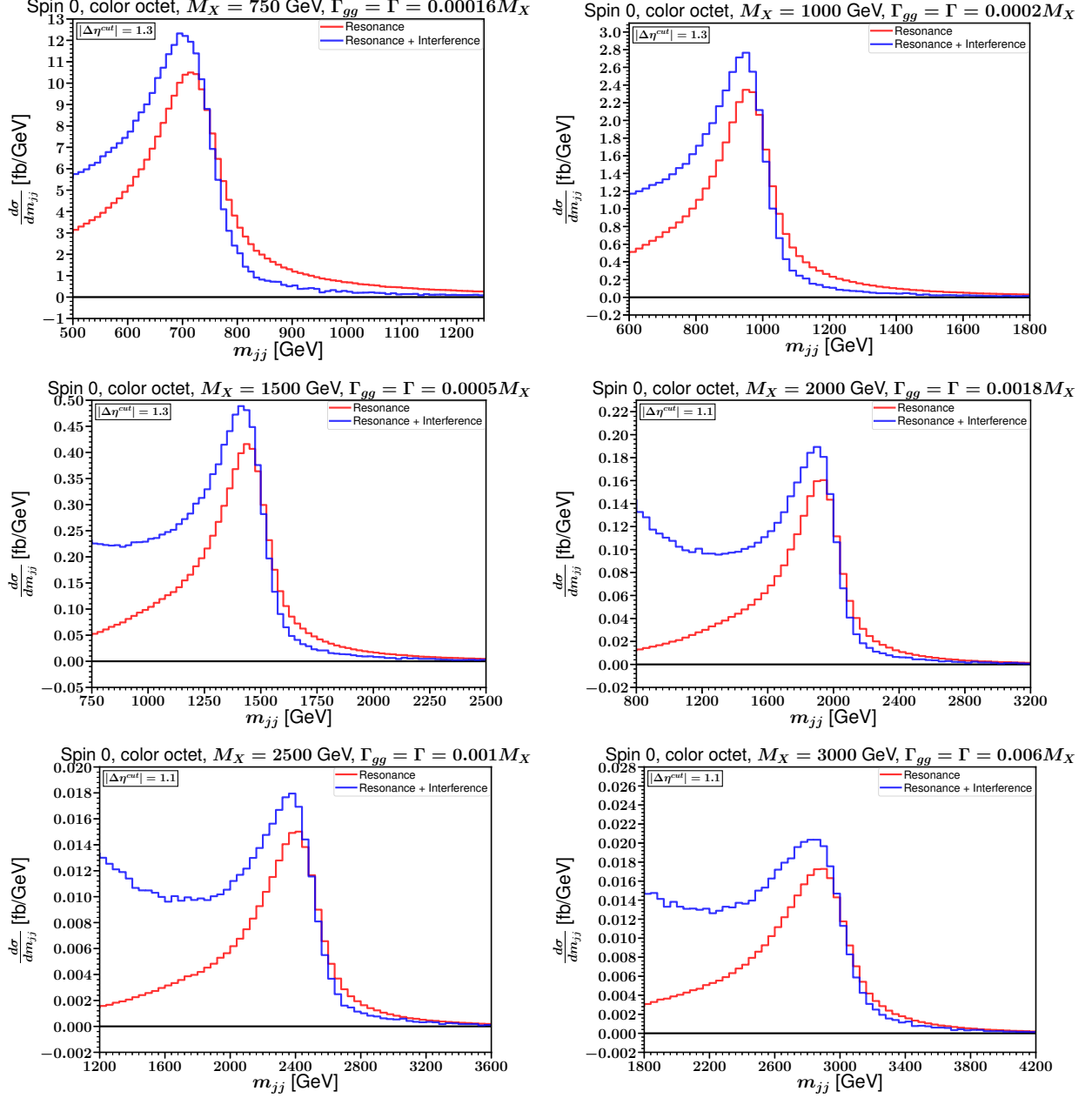
FIG. 4.4: Dijet invariant mass distributions for the spin-0, color-octet benchmarks of Table 2.1 with $\Gamma = \Gamma_{gg}$, at the 13 TeV LHC, obtained with showering, hadronization and detector simulation. The red lines show the naive results with the resonance diagrams of $gg \to X \to gg$ process (RES), which include the s-, t-, and u-channel exchanges of X, while the blue lines show the full results including interferences with the continuum QCD $gg \to gg$ amplitudes (INT). The cases shown in the right column can be compared directly to those in the right column of the previous Figure 4.3 based on the more simplistic method of parton level with smearing.

C. Spin 1, color octet

1. Parton-level with smearing

Figure 4.5 shows the digluon invariant mass distributions, for pp collisions at $\sqrt{s} = 13$ TeV, for spin-1 color-octet resonances with benchmark examples of Table 2.1, namely $(M_X, \Gamma/M_X) = (1000$ GeV, $6.5 \times 10^{-5})$ [top row], $(2000$ GeV, $5.4 \times 10^{-4})$ [middle row] and $(3000$ GeV, $0.00183)$ [bottom row]. As before, the parton-level results before smearing are shown in the left panels, and the corresponding mass distributions after smearing are shown in the right panels. In all panels, the red lines show the results for the resonant signal $gg \to X \to gg$ with all s, t, u-channel X exchange diagrams, while the blue lines show the full results including the interferences with the QCD background $gg \to gg$. In this case, the relative effects of the interference are seen to be of a similar character, but smaller than, the spin-0 cases discussed above.

2. Monte Carlo results with showering, hadronization, and detector simulation

Figure 4.6 shows all of the the dijet invariant mass distributions for the considered benchmarks of Table 2.1 with $\Gamma = \Gamma_{gg}$, at 13 TeV LHC, for spin-1, color-octet resonances, obtained using Monte Carlo simulations. The results are shown for a digluon resonant process $gg \to X \to gg$, and the full results, which also include the interferences with the continuum QCD $gg \to gg$ amplitudes.

From Figure 4.6 we see that the QCD interferences with spin-1, color-octet (blue lines) has a peak below the resonance mass, which is almost comparable to the pure peak, obtained by excluding the interference terms. The differential cross sections in the region $m_{jj} > M_X$ are almost unaffected by including the interference. However, as before, the presence of the large low-mass tail means that after fitting the QCD background, the residual distribution may have an apparent deficit of events above M_X. Comparing the right columns of Figures 4.5 and 4.6, we note that in this case the difference between the shapes found with the parton-level smearing method and the full event simulation method is more significant than in the spin-0 case, this time with a larger yield and a more pronounced low mass tail using the latter, presumably more accurate, method. As was the case with the color-singlet resonances, the QCD interference seems to have relatively larger impact at higher resonance masses than at smaller M_X.
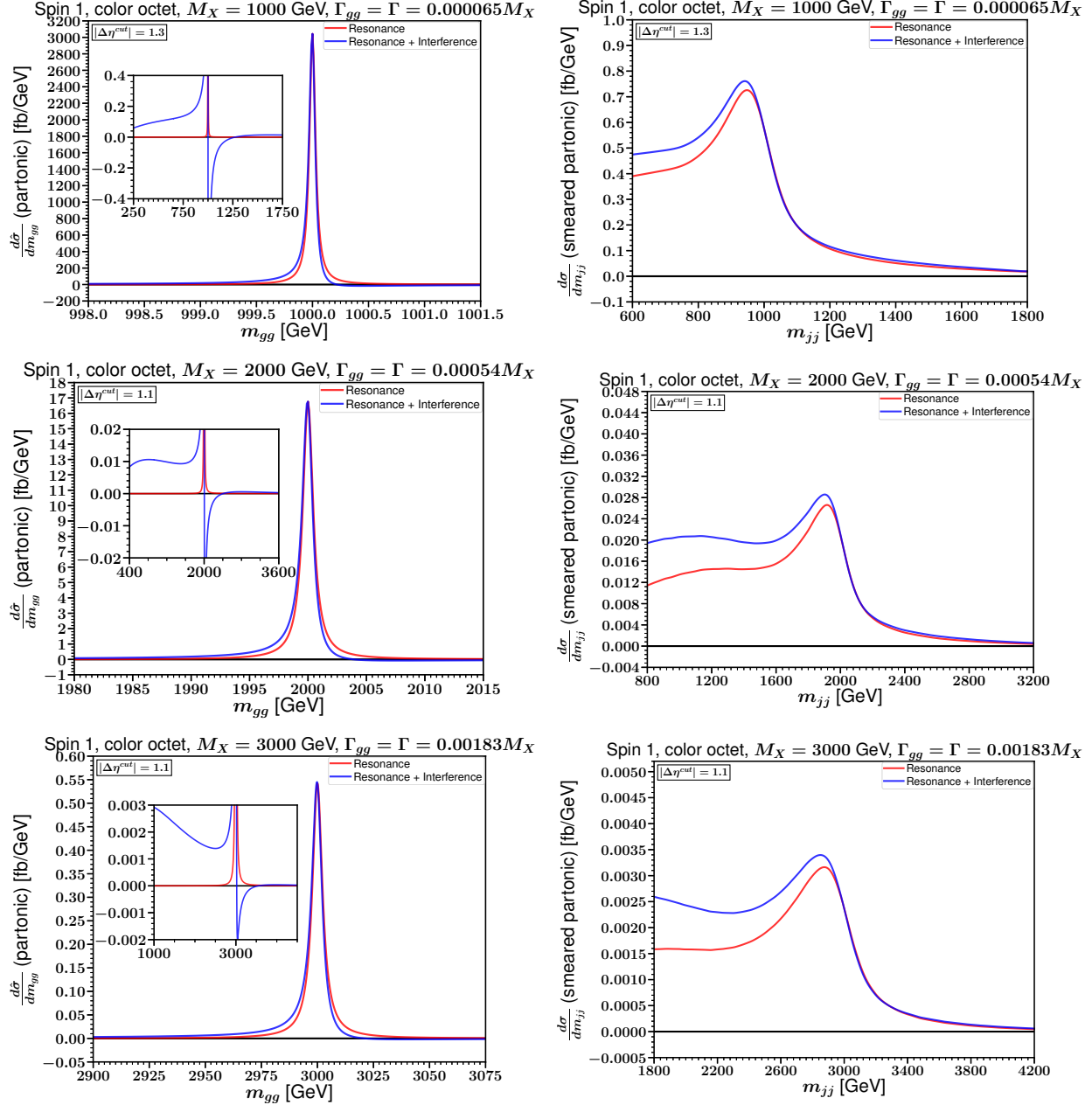
FIG. 4.5: Digluon invariant mass distributions, at the 13 TeV LHC, for spin-1 color-octet resonances with $(M_X, \Gamma/M_X) = (1000 \text{ GeV}, 6.5 \times 10^{-5})$ [top row], $(2000 \text{ GeV}, 5.4 \times 10^{-4})$ [middle row] and $(3000 \text{ GeV}, 0.00183)$ [bottom row]. The parton-level distributions (left panels) are smeared by convolution with the detector response, shown in Figure 3.1, to obtain the dijet invariant mass distributions (right panels). In all six panels, the red lines show the naive results for the resonant signal $gg \to X \to gg$, while the blue lines show the full results including the interferences with the QCD background $gg \to gg$. The inset plots within the left panels and their enclosing plots show the same data but with different scales on the axes.
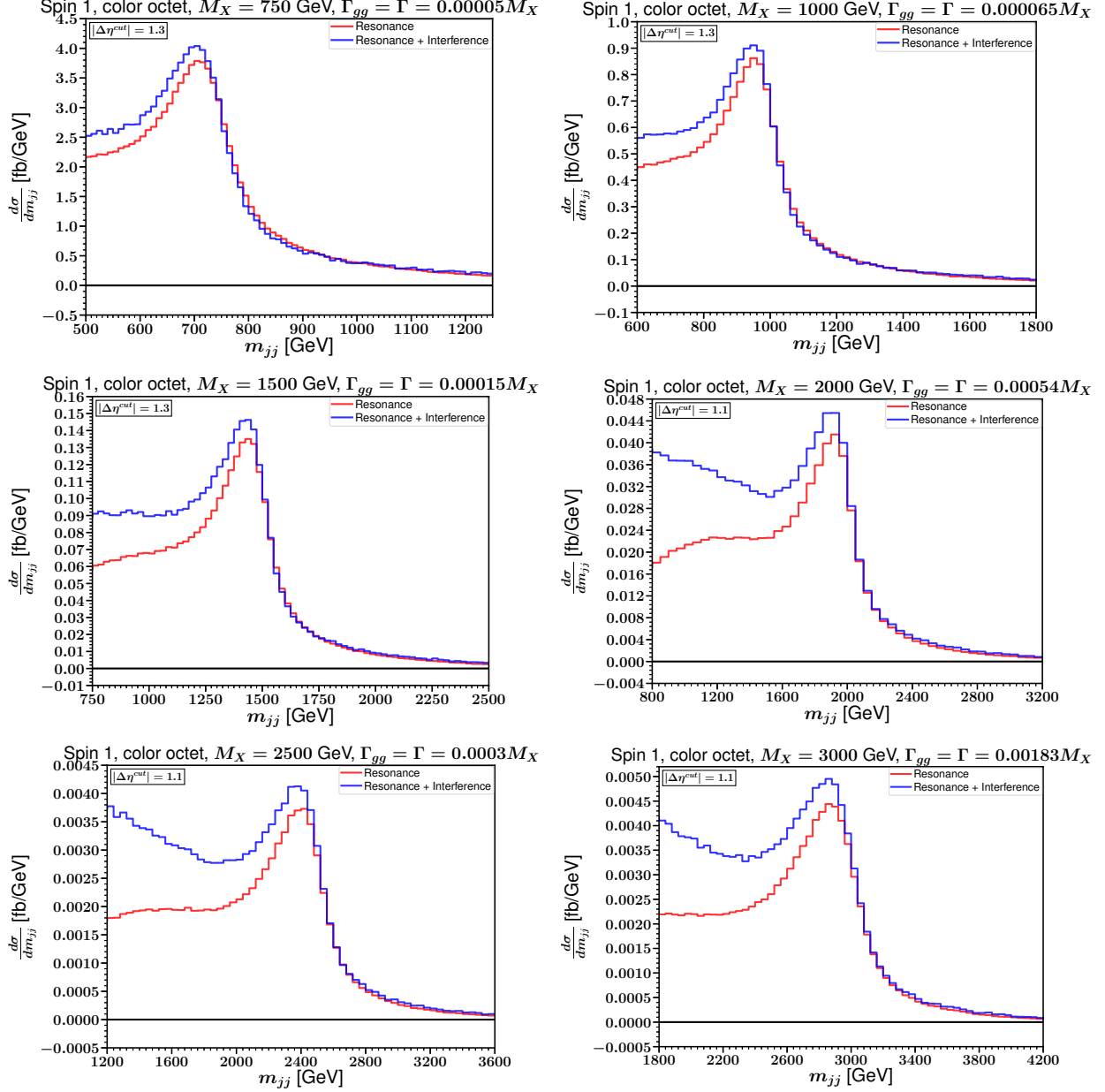
FIG. 4.6: Dijit invariant mass distributions for the spin-1 color-octet benchmarks of Table 2.1 with $\Gamma = \Gamma_{gg}$, at the 13 TeV LHC, obtained with showering, hadronization and detector simulation. The red lines show the naive results with the resonance diagrams of $gg \to X \to gg$ process (RES), which include the s-, t-, and u-channel exchanges of X, while the blue lines show the full results including interferences with the continuum QCD $gg \to gg$ amplitudes (INT). The cases shown in the right column can be compared directly to those in the right column of the previous Figure 4.5 based on the more simplistic method of parton level with smearing.

D.   Spin 2, color singlet

1.   Parton-level with smearing

We now turn to the case of a massive spin-2, color-singlet digluon resonance. In Figure 4.7, we show the parton-level digluon invariant mass distributions for pp collisions at $\sqrt{s} = 13$ TeV, for $(M_X, \Gamma/M_X) = (1000 \text{ GeV}, 0.00041)$ [top row], $(2000 \text{ GeV}, 0.00375)$ [middle row], and $(3000 \text{ GeV}, 0.014)$ [bottom row]. As before, the results before smearing are shown in the left panels, and mass distributions after smearing are shown in the right panels. In all panels, the red lines show the results for the resonant signal $gg \to X \to gg$ with all X exchange diagrams, while the blue lines show the full results including the interferences with the QCD $gg \to gg$ amplitudes.

In the spin-2 case, we note that there is a unique feature not found in the previous cases: the effect of the interference is negative for all dijet invariant masses well below M_X after smearing (but with a magnitude that of course varies with the mass). This can be traced in part to a large negative interference effect in the parton-level results for m_{gg} well below M_X, due to the contributions from the interference between t-, and u-channel X exchange diagrams and the QCD diagrams. Thus, at the parton level for spin-2 color-singlets, there is an interference dip in the regions $m_{gg} \ll M_X$ (although it is small compared to the large QCD background in that range of m_{gg}). This translates into a substantial negative low-mass tail compared to the naive pure resonance result. There is then a steady rise until m_{jj} is slightly less than M_X, followed by a dip in the regions $m_{jj} > M_X$. It would be interesting to see whether this pattern is maintained after including higher order contributions.

2.   Monte Carlo results with detector simulation

Figure 4.8 shows the dijet invariant mass distributions for the spin-2, color-singlet resonance benchmarks of Table 2.1 with $\Gamma = \Gamma_{gg}$, at 13 TeV LHC, obtained using Monte Carlo simulations. The results are shown for a digluon resonant process $gg \to X \to gg$, and the full results, which also include the interferences with the continuum QCD $gg \to gg$ amplitudes for all four color flows shown in Figure 3.2.

As was the case with the color-singlet scalars, from Figure 4.8, the interference effects have the least impact for the color flow that we call X_s. On the other hand, interference effects are more pronounced for the t/u-channel color flow of both QCD and resonant processes. Also, we confirm that QCD interferences have negative cross section for smaller invariant masses $m_{jj} \ll M_X$. Then, similar to the case of spin-0 color-singlet resonances, there is a peak/dip pattern around the resonance mass $m_{jj} \approx M_X$, in agreement with the results at parton-level with smearing found in Fig. 4.7. The net effect of negative interference both above and below the M_X means that, after fitting to the QCD background, the resonance peak could actually stand out more prominently than predicted by the naive pure-resonance prediction. Once again, the relative importance of the interference for $m_{jj} < M_X$ increases with M_X.
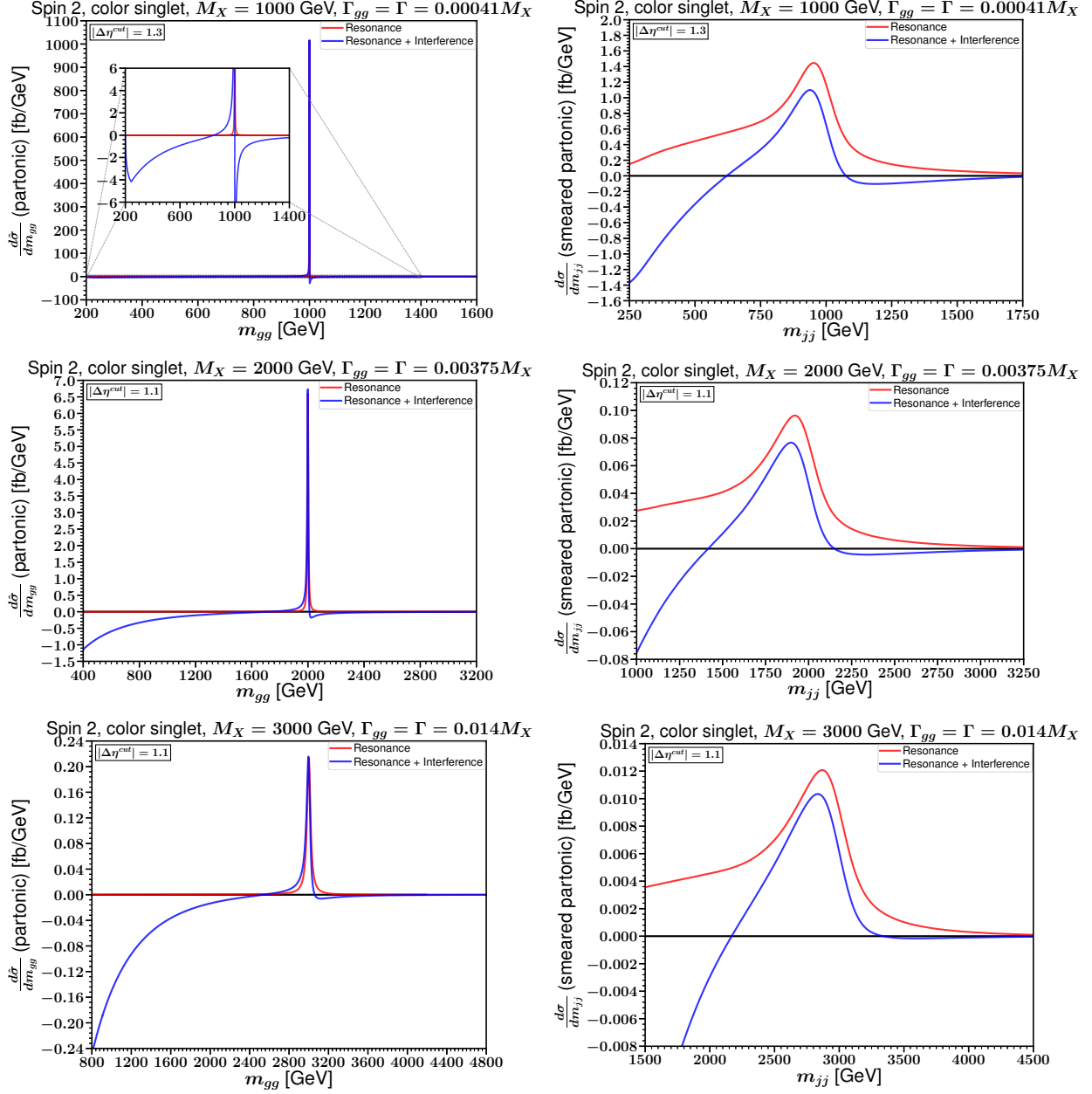
FIG. 4.7: Digluon invariant mass distributions, at the 13 TeV LHC, for spin-2, color-singlet resonances with $(M_X, \Gamma/M_X) = (1000$ GeV, $0.00041)$ [top row], $(2000$ GeV, $0.00375)$ [middle row], and $(3000$ GeV, $0.014)$ [bottom row]. The parton-level distributions (left panels) are smeared by convolution with the detector response, shown in Figure 3.1, to obtain the dijet invariant mass distributions (right panels). In all six panels, the red lines show the naive results for the resonant signal $gg \to X \to gg$, while the blue lines show the full results including the interferences with the QCD background $gg \to gg$. The inset plot within the top-left panel shows the same data as its enclosing plot but with different scales on the axes. The negative tails at small invariant mass come from the interference between the QCD amplitudes and the t- and u-channel X exchange diagrams.
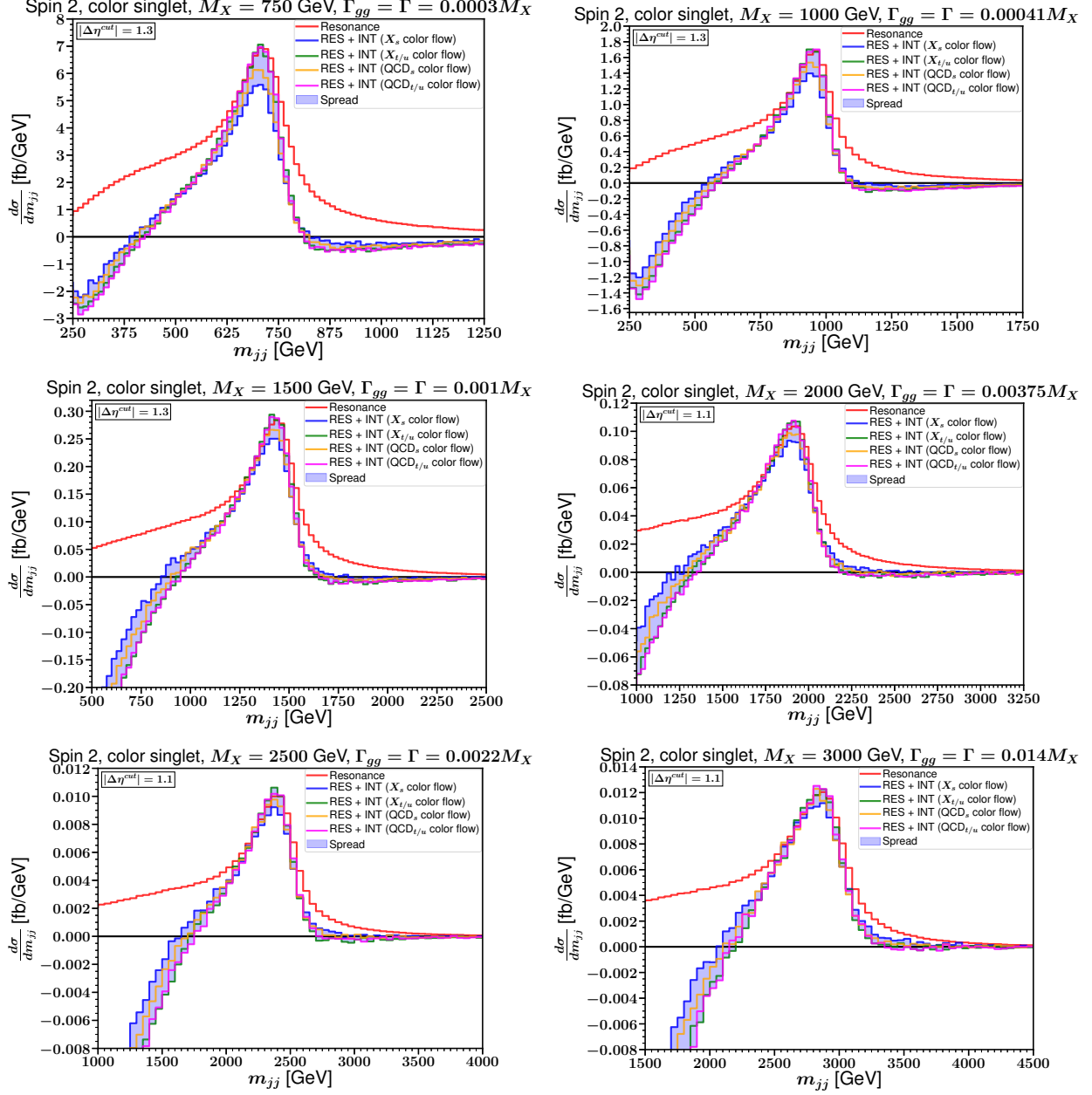
FIG. 4.8: Dijet invariant mass distributions for the spin-2, color-singlet resonance benchmarks of Table 2.1 with $\Gamma = \Gamma_{gg}$, at 13 TeV LHC, obtained with showering, hadronization and detector simulation. The red lines show the naive results with the resonance diagrams of $gg \to X \to gg$ process (RES), which include the s-, t-, and u-channel exchanges of X, while the other four colored lines show the full results including interferences with the continuum QCD $gg \to gg$ amplitudes (INT) for all four color flows shown in Figure 3.2, as labeled. The shaded region shows the spread in the full result in each invariant mass bin, for the four different color flow choices. The negative tails at small invariant mass come from the interference between the QCD amplitudes and the t- and u-channel X exchange diagrams. The cases shown in the right column can be compared directly to those in the right column of the previous Figure 4.7 based on the more simplistic method of parton level with smearing.

V.   RESULTS FOR $\Gamma = 5\Gamma_{gg}$

As noted in ref. [55], the interference effects are expected to be relatively enhanced for smaller branching ratios $\mathrm{BR}(X \to gg) = \Gamma_{gg}/\Gamma$, for a given fixed resonant production cross-section. The reason for this is that to reach the same cross-section, both Γ_{gg} and Γ must be larger than if they were equal [see eq. (2.21)], leading to much larger Breit-Wigner tails away from the resonance region, which then produce larger interference with the QCD amplitude. Thus, the case with $\Gamma = \Gamma_{gg}$ studied above actually has the minimal impact on the interference with QCD, compared to the general case $\Gamma_{gg} < \Gamma$. In this section, we illustrate this by considering, somewhat arbitrarily, the case that $\Gamma_{gg} = \Gamma/5$.

The organization of results and structure of the figures below is exactly the same as in the previous section. Thus in Figures 5.1, 5.3, 5.5, and 5.7, we show the parton-level distributions before (left columns) and after (right columns) smearing by convolution with the detector response functions illustrated in Figure 3.1, for benchmark masses 1000 GeV (top rows), 2000 GeV (middle rows), and 3000 GeV (bottom rows). For $\Gamma_{gg} = \Gamma/5$, the benchmark width-to-mass ratios turn out to be very large for a few cases considered here. For example, $\Gamma/M_X = (1.75, 0.475)$ for a spin-0 color-singlet with $M_X = (3000, 2000)$ GeV, and $\Gamma/M_X = 0.35$ for a spin-2 color-singlet with $M_X = 3000$ GeV. The case with $\Gamma/M_X = 1.75$ for a 3000 GeV massive color-singlet (pseudo-)scalar has unrealistically large width-to-mass ratio for a resonance, and is therefore omitted. On the other hand, cases with a large width-to-mass ratio but with $\Gamma/M_X < 0.55$ are not omitted as the CMS experiment has considered broad resonances with widths up to 55% of the resonance mass in the reference [2].

In Figures 5.2, 5.4, 5.6, and 5.8, we show the results obtained by our full event simulation including showering, hadronization, and detector simulation. The right columns of pairs of figures (5.1 and 5.2 for spin-0 color-singlet, 5.3 and 5.4 for spin-0 color-octet, 5.5 and 5.6 for spin-1 color-octet, and 5.7 and 5.8 for spin-2 color-singlet) can be directly compared, as they feature the same masses and widths. The agreement between these sets of figures appears to be good at the qualitative level, but with differing yields at up to the level of tens of percent, and somewhat different shapes in some cases. In particular, for spin 1, the full event simulation produces larger low-mass tails than the smeared parton-level results. In addition, the color-flow choice in the color-singlet interference cases is seen to be a non-trivial effect.

A general feature that can be seen in all of these figures is that when $\Gamma_{gg} = \Gamma/5$, the distributions including interference can bear little resemblance to the naive resonance-only results. In each of the spin-0 and spin-1 cases, there is a very large low-mass tail from the interference. For lower M_X and spin-0, we find a pronounced dip for m_{jj} above M_X, but this tends to be washed out for larger M_X and higher spin. In practice, the falling distribution well below M_X will be partly absorbed into the QCD background fit, and, if present, can therefore have a significant effect on that fit. The result could be a peak/dip or dip shape in the residual fit. We note that the magnitude of the effective dip after background fitting could easily be as large or larger than the peak that would be naively expected from the resonance if one ignored the interference effect. We also emphasize that the low-mass tail from interference is much larger than the width effect in the pure resonant contribution (visible as the broad distribution of the red curves). The latter effect has been considered
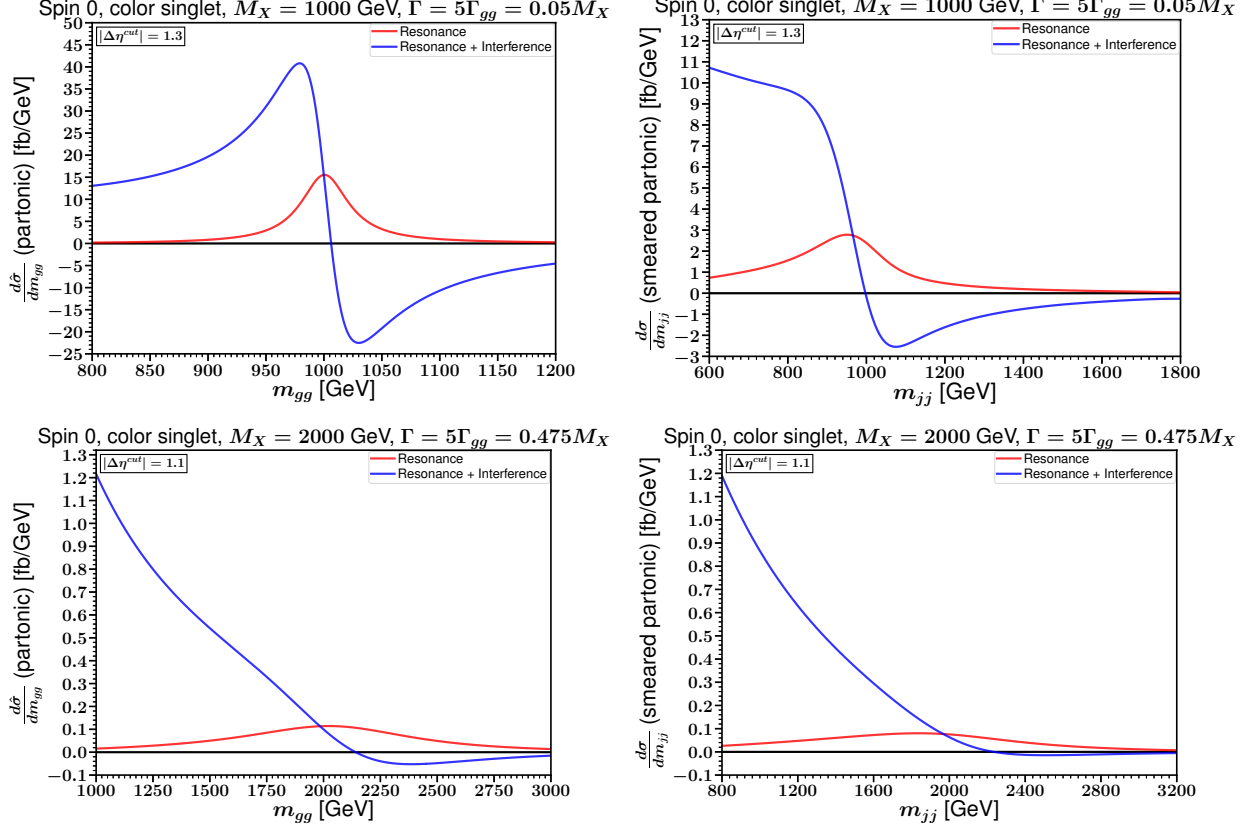
FIG. 5.1: Digluon invariant mass distributions, at the 13 TeV LHC, for benchmark spin-0, color-singlet resonances from Table 2.1, with $\Gamma_{gg} = \Gamma/5$, and $M_X = 1000$ GeV (top row), and 2000 GeV (bottom row). The parton-level distributions are shown in the left column panels. These are are then smeared by convolution with the estimated detector responses shown in Figure 3.1 to obtain the dijet invariant mass distributions in the right column panels. In all four panels, the red lines show the naive results for the resonant signal $gg \to X \to gg$, while the blue lines show the full results including the interferences with the QCD background $gg \to gg$.

in experimental searches [1, 2] with $\Gamma > \Gamma_{gg}$, but the much larger former effect has not.

In the spin-2 color-singlet case (see Figure 5.8), the distribution shape tends to feature a large deficit at low masses, a peak just below M_X, and then another deficit above M_X. After fitting the QCD background, this should lead to an enhancement of the peak compared to the naive resonance-only distribution, so we expect that the actual limits attainable would likely be stronger than those inferred without considering interference.
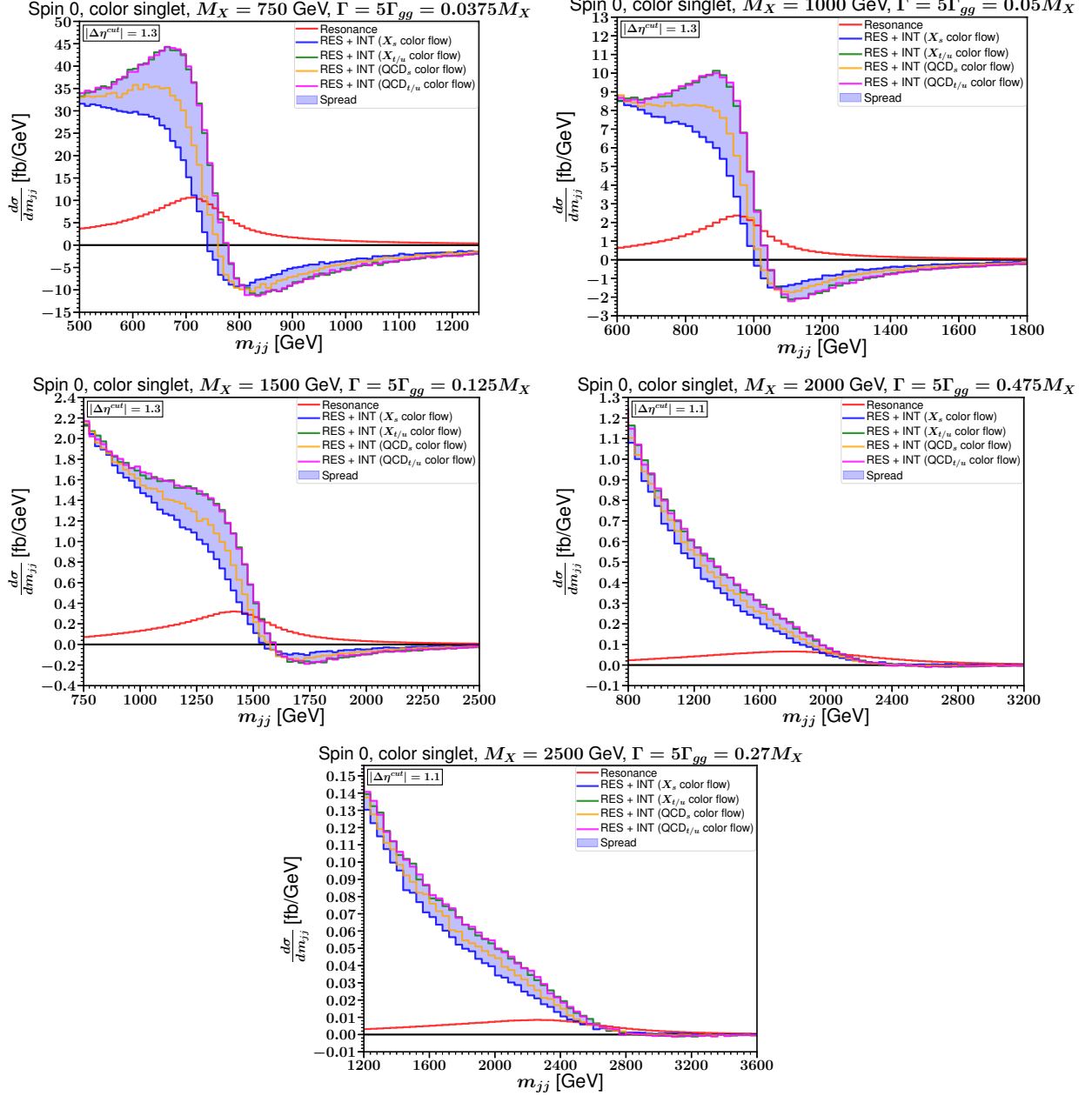
FIG. 5.2: Dijet invariant mass distributions for the spin-0, color-singlet benchmarks of Table 2.1 with $\Gamma_{gg} = \Gamma/5$, at the 13 TeV LHC, obtained with showering, hadronization and detector simulation. The red lines show the naive results with only the resonance diagrams of $gg \to X \to gg$ process (RES), which include the s-, t-, and u-channel exchanges of X, while the other four lines show the full results including interferences with the continuum QCD $gg \to gg$ amplitudes (INT) for all four color flows shown in Figure 3.2, as labeled. The shaded region shows the spread in the full result in each invariant mass bin for the different color flow choices. The cases shown in the right column of the top and the middle rows can be compared directly to those in the right column of the previous Figure 5.1 based on the more simplistic method of parton level with smearing.
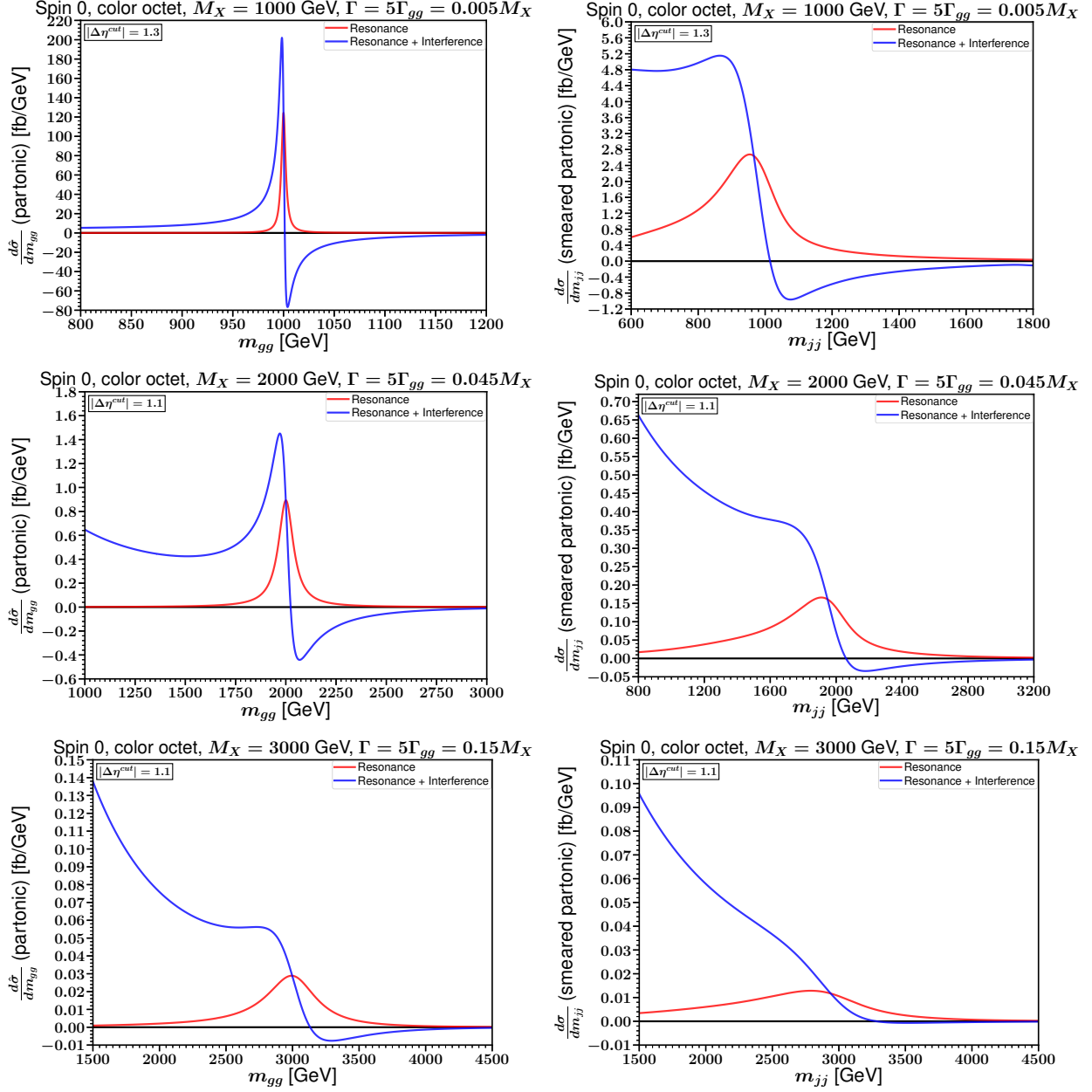
FIG. 5.3: Digluon invariant mass distributions, at the 13 TeV LHC, for benchmark spin-0, color-octet resonances from Table 2.1, with $\Gamma_{gg} = \Gamma/5$, and $M_X = 1000$ GeV (top row), and 2000 GeV (middle row) and 3000 GeV (bottom row). The parton-level distributions are shown in the left column panels. These are are then smeared by convolution with the estimated detector responses shown in Figure 3.1 to obtain the dijet invariant mass distributions in the right column panels. In all six panels, the red lines show the naive results for the resonant signal $gg \to X \to gg$, while the blue lines show the full results including the interferences with the QCD background $gg \to gg$.
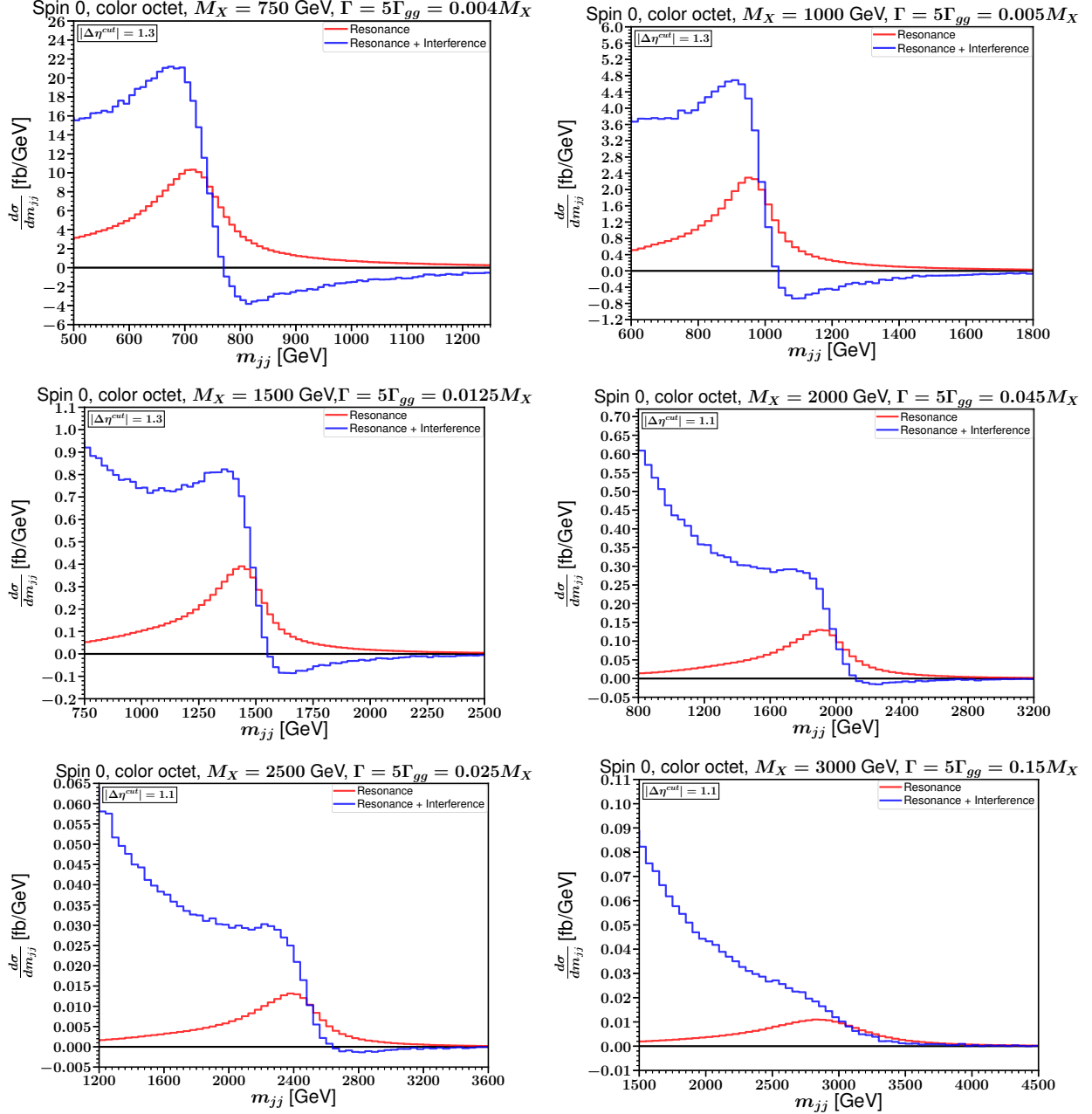
FIG. 5.4: Dijet invariant mass distributions for the spin-0, color-octet benchmarks of Table 2.1 with $\Gamma_{gg} = \Gamma/5$, at the 13 TeV LHC, obtained with showering, hadronization and detector simulation. The red lines show the naive results with only the resonance diagrams of $gg \to X \to gg$ process (RES), which include the s-, t-, and u-channel exchanges of X, while the blue lines show the full results including interferences with the continuum QCD $gg \to gg$ amplitudes (INT). The cases shown in the right column can be compared directly to those in the right column of the previous Figure 5.3 based on the more simplistic method of parton level with smearing.
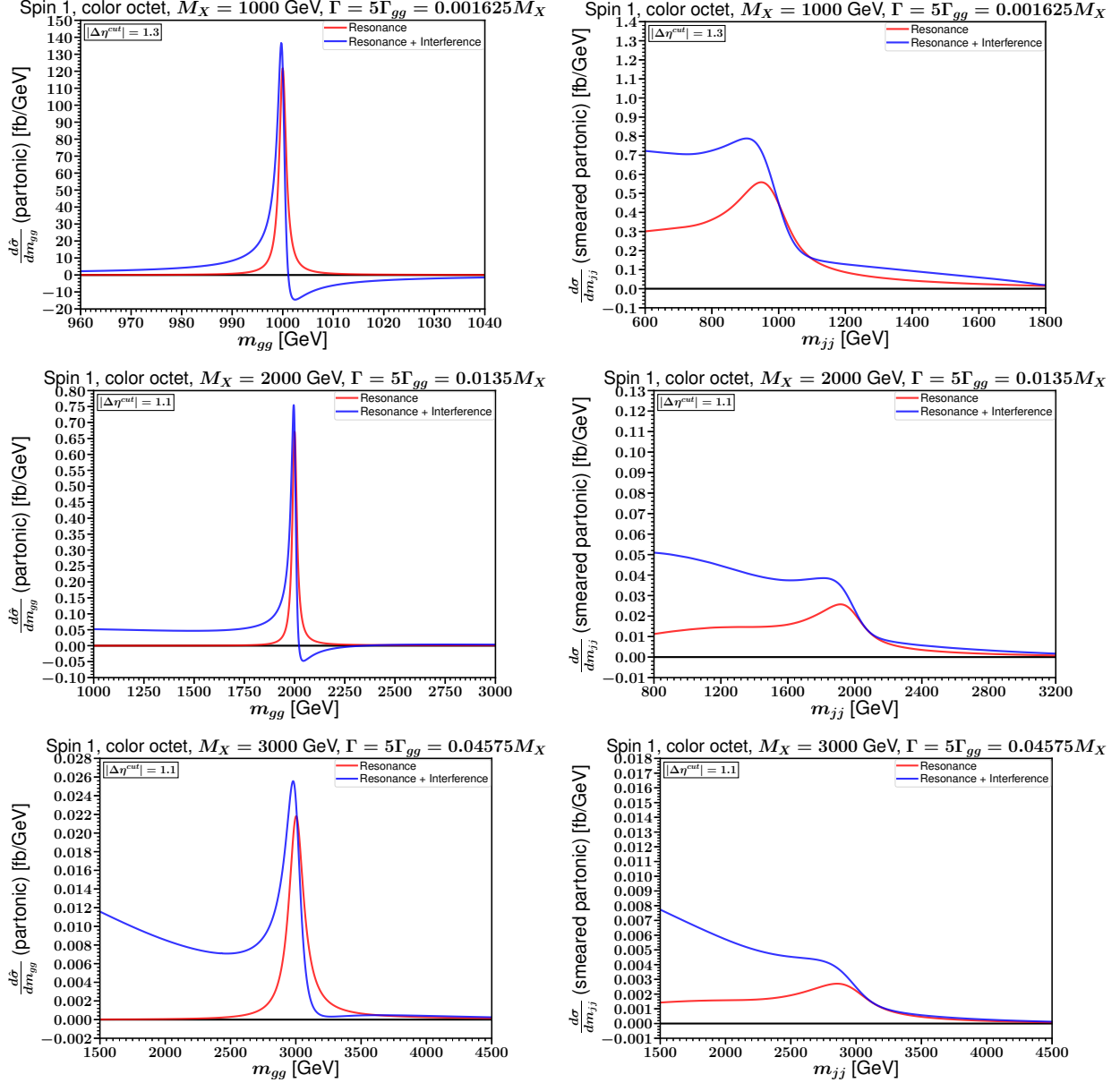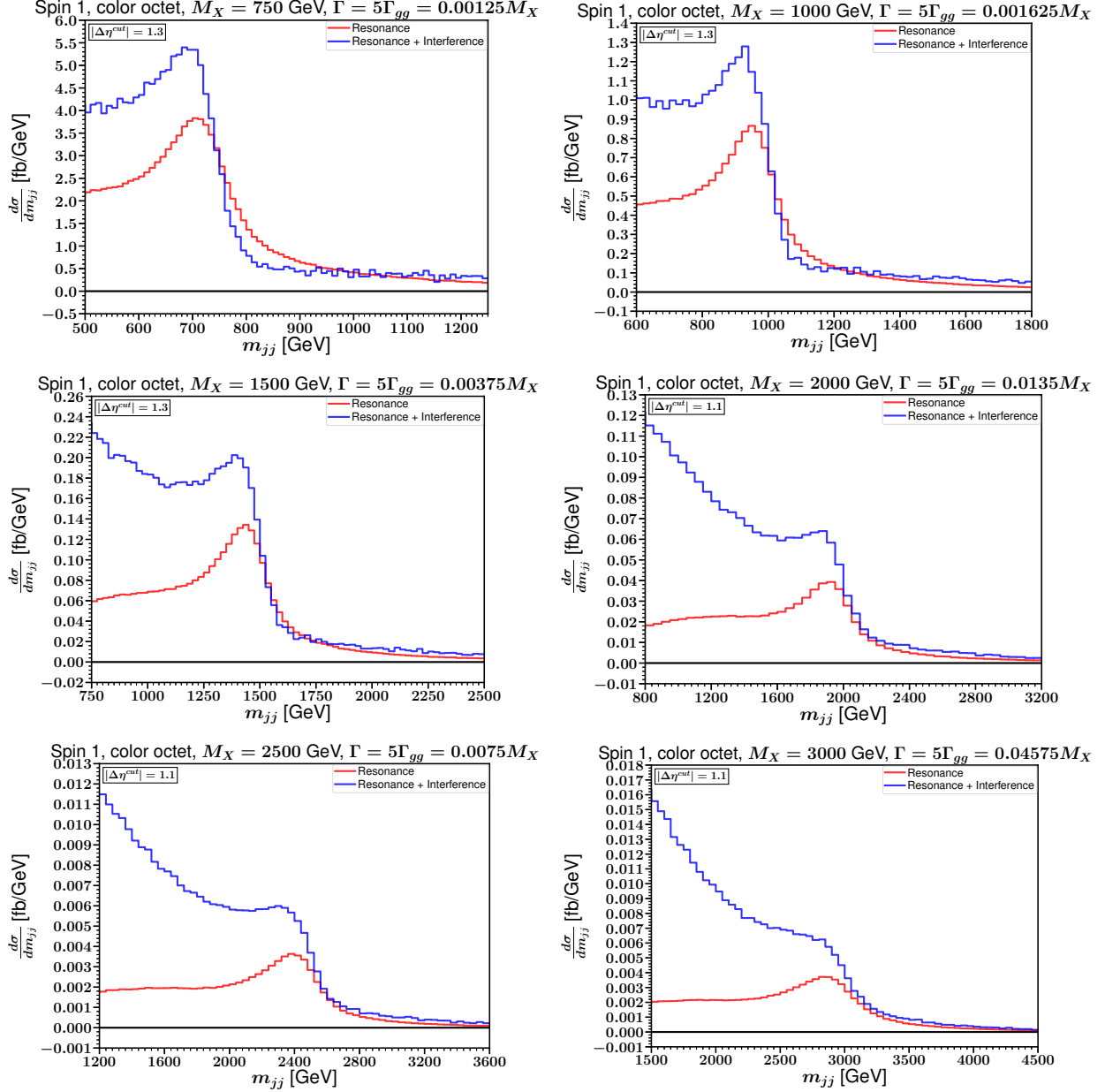
FIG. 5.5: Digluon invariant mass distributions, at the 13 TeV LHC, for benchmark spin-1, color-octet resonances from Table 2.1, with $\Gamma_{gg} = \Gamma/5$, and $M_X = 1000$ GeV (top row), and 2000 GeV (middle row) and 3000 GeV (bottom row). The parton-level distributions are shown in the left column panels. These are are then smeared by convolution with the estimated detector responses shown in Figure 3.1 to obtain the dijet invariant mass distributions in the right column panels. In all six panels, the red lines show the naive results for the resonant signal $gg \to X \to gg$, while the blue lines show the full results including the interferences with the QCD background $gg \to gg$.

FIG. 5.6: Dijet invariant mass distributions for the spin-1, color-octet benchmarks of Table 2.1 with $\Gamma_{gg} = \Gamma/5$, at the 13 TeV LHC, obtained with showering, hadronization and detector simulation. The red lines show the naive results with only the resonance diagrams of $gg \to X \to gg$ process (RES), which include the s-, t-, and u-channel exchanges of X, while the blue lines show the full results including interferences with the continuum QCD $gg \to gg$ amplitudes (INT). The cases shown in the right column can be compared directly to those in the right column of the previous Figure 5.5 based on the more simplistic method of parton level with smearing.
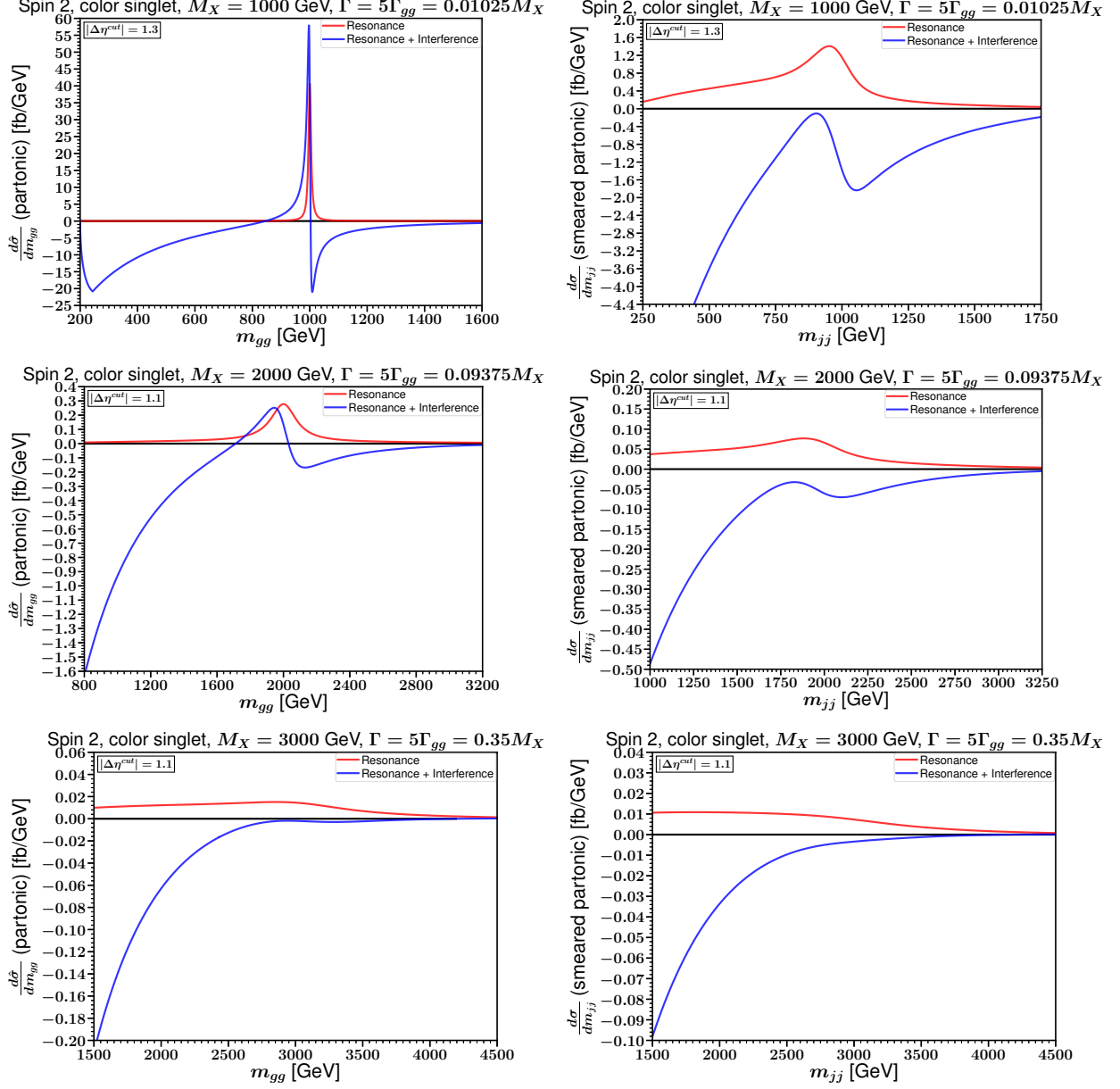
FIG. 5.7: Digluon invariant mass distributions, at the 13 TeV LHC, for benchmark spin-2, color-singlet resonances from Table 2.1, with $\Gamma_{gg} = \Gamma/5$, and $M_X = 1000$ GeV (top row), and 2000 GeV (middle row) and 3000 GeV (bottom row). The parton-level distributions are shown in the left column panels. These are are then smeared by convolution with the estimated detector responses shown in Figure 3.1 to obtain the dijet invariant mass distributions in the right column panels. In all six panels, the red lines show the naive results for the resonant signal $gg \to X \to gg$, while the blue lines show the full results including the interferences with the QCD background $gg \to gg$. The negative tails at small invariant mass come from the interference between the QCD amplitudes and the t- and u-channel X exchange diagrams.
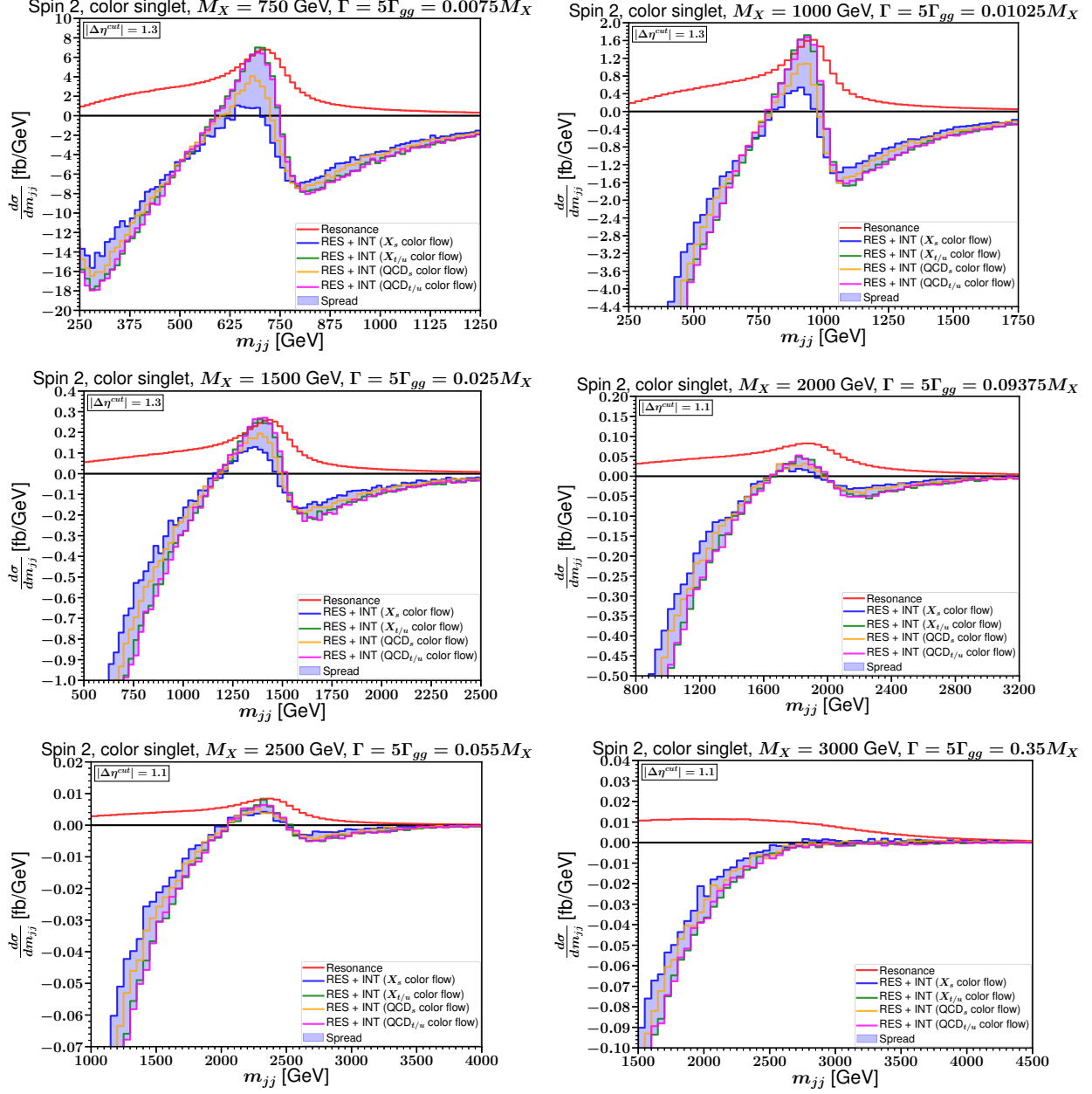
FIG. 5.8: Dijet invariant mass distributions for the spin-2, color-singlet benchmarks of Table 2.1 with $\Gamma_{gg} = \Gamma/5$, at the 13 TeV LHC, obtained with showering, hadronization and detector simulation. The red lines show the naive results with only the resonance diagrams of $gg \to X \to gg$ process (RES), which include the s-, t-, and u-channel exchanges of X, while the other four colored lines show the full results including interferences with the continuum QCD $gg \to gg$ amplitudes (INT) for all four color flows shown in Figure 3.2, as labeled. The shaded region shows the spread in the full result in each invariant mass bin for the different color flow choices. The negative tails at small invariant mass come from the interference between the QCD amplitudes and the t- and u-channel X exchange diagrams. The cases shown in the right column can be compared directly to those in the right column of the previous Figure 5.7 based on the more simplistic method of parton level with smearing.

VI. OUTLOOK

In this paper, we studied the importance of the interference between the digluon resonant signal and the QCD background amplitude in LHC searches. We showed that the interference terms change the naive Breit-Wigner resonance peak to more like a peak-dip structure around the resonance mass. However, the particular characteristic shape depends on the spin and the color of the digluon resonance. The interference effects were studied for scalar and pseudo-scalar resonances in both singlet and octet color representations, spin-1 color-octets, and color-singlet massive gravitons. To show the importance of the interference effects, we considered a few benchmark examples for various resonance masses, such that their production cross sections are close to the claimed exclusions of the CMS experiment in refs. [1, 2].

We found that the effects of interference were larger for the spin-0 color singlet case than for the spin-0 color-octet and spin-1 color-octet cases, as was expected from consideration of the parton-level differential cross-sections. We also note that the relative impact of the interference stays nearly constant for a fixed M_X as the resonant cross-section decreases, but tends to increase for larger M_X. It can also increase dramatically if the resonance has other decays contributing to its width that are not detectable for some reason. Our results still contain significant uncertainties, in particular from the color-flow ambiguities in the color-singlet cases, and from the fact that in this paper we have not included any NLO effects. It would be interesting to go beyond the approximations used in this paper in order to reduce these sources of uncertainty.

After performing a fit to the QCD background, the residual signal for a digluon resonance could have a shape in the invariant mass distribution that appears to resemble a peak/dip, a shelf, an enhanced peak, or even a pure dip. For all cases except spin-2, there is a large positive tail at invariant masses below M_X. Because the magnitude of the QCD background amplitude falls with $\sqrt{\hat{s}}$, the low-mass tail tends to be more significant than the high-mass deficit from the interference. In the spin-2 case, we found that the low mass tail is larger in magnitude but actually switches signs, and is negative far below M_X, due to interference between the QCD background and the t- and u-channel X exchange. After QCD fitting and subtraction, this could lead to an enhanced peak in the spin-2 case, compared to the naive pure-resonance distribution expected if one neglects the interference.

More generally, the results found here point to the appropriateness of a flexible approach to searching for dijet resonances. Although one is searching for a resonance, we have seen that there is a considerable diversity of possible invariant mass distribution signals even for resonances with rather narrow widths, depending on the resonance quantum numbers, width, and branching ratios, as can be seen from the figures above. Perhaps advanced data analysis and machine learning techniques can be brought to bear on the problem of identifying or setting limits on new-physics anomalies in mass distributions in a general and efficient way (see, for example, refs. [120–124] for recent developments). In any case, it seems necessary to consider a variety of possible anomalies in the dijet mass distribution, without undue prejudice towards a simple resonance peak.

---

[1] A. M. Sirunyan *et al.* [CMS Collaboration], "Search for narrow and broad dijet resonances in proton-proton collisions at $\sqrt{s} = 13$ TeV and constraints on dark matter mediators and other new particles," JHEP **1808**, 130 (2018) doi:10.1007/JHEP08(2018)130 [arXiv:1806.00843 [hep-ex]].

[2] A. M. Sirunyan *et al.* [CMS Collaboration], "Search for high mass dijet resonances with a new background prediction method in proton-proton collisions at $\sqrt{s} = 13$ TeV," arXiv:1911.03947 [hep-ex].

[3] M. Aaboud *et al.* [ATLAS Collaboration], "Search for new phenomena in dijet events using 37 fb^{-1} of pp collision data collected at $\sqrt{s} =$13 TeV with the ATLAS detector," Phys. Rev. D **96**, no. 5, 052004 (2017) doi:10.1103/PhysRevD.96.052004 [arXiv:1703.09127 [hep-ex]].

[4] G. Aad *et al.* [ATLAS Collaboration], "Search for new resonances in mass distributions of jet pairs using 139 fb^{-1} of pp collisions at $\sqrt{s} = 13$ TeV with the ATLAS detector," arXiv:1910.08447 [hep-ex].

[5] S. Chatrchyan *et al.* [CMS Collaboration], "Search for Narrow Resonances Using the Dijet Mass Spectrum in pp Collisions at $\sqrt{s}$=8 TeV," Phys. Rev. D **87**, no. 11, 114015 (2013) [arXiv:1302.4794 [hep-ex]].

[6] G. Aad *et al.* [ATLAS Collaboration], "Search for new phenomena in the dijet mass distribution using $p - p$ collision data at $\sqrt{s} = 8$ TeV with the ATLAS detector," Phys. Rev. D **91**, no. 5, 052007 (2015) [arXiv:1407.1376 [hep-ex]].

[7] V. Khachatryan *et al.* [CMS Collaboration], "Search for resonances and quantum black holes using dijet mass spectra in proton-proton collisions at $\sqrt{s} = 8$ TeV," Phys. Rev. D **91**, no. 5, 052009 (2015) [arXiv:1501.04198 [hep-ex]].

[8] V. Khachatryan *et al.* [CMS Collaboration], "Search for narrow resonances in dijet final states at $\sqrt{(s)} = 8$ TeV with the novel CMS technique of data scouting," Phys. Rev. Lett. **117**, no. 3, 031802 (2016) [arXiv:1604.08907 [hep-ex]].

[9] G. Aad *et al.* [ATLAS Collaboration], "Search for new phenomena in dijet mass and angular distributions from pp collisions at $\sqrt{s} = 13$ TeV with the ATLAS detector," Phys. Lett. B **754**, 302 (2016) [arXiv:1512.01530 [hep-ex]].

[10] V. Khachatryan *et al.* [CMS Collaboration], "Search for narrow resonances decaying to dijets in proton-proton collisions at $\sqrt{(s)} = 13$ TeV," Phys. Rev. Lett. **116**, no. 7, 071801 (2016) [arXiv:1512.01224 [hep-ex]].

[11] A. M. Sirunyan *et al.* [CMS Collaboration], "Search for dijet resonances in proton?proton collisions at $\sqrt{s} = 13$ TeV and constraints on dark matter and other models," Phys. Lett. B **769**, 520 (2017) Erratum: [Phys. Lett. B **772**, 882 (2017)] [arXiv:1611.03568 [hep-ex]].

[12] P. H. Frampton and S. L. Glashow, "Chiral Color: An Alternative to the Standard Model," Phys. Lett. B **190**, 157 (1987). doi:10.1016/0370-2693(87)90859-8

[13] P. H. Frampton and S. L. Glashow, "Unifiable Chiral Color With Natural GIM Mechanism," Phys. Rev. Lett. **58**, 2168 (1987). doi:10.1103/PhysRevLett.58.2168

[14] P. H. Frampton, "Alternative Version of Chiral Color as Alternative to the Standard Model," Phys. Rev. D **81**, 095005 (2010) doi:10.1103/PhysRevD.81.095005 [arXiv:0910.0307 [hep-ph]].

[15] J. C. Pati and A. Salam, "Mirror Fermions, J/psi Particles, Kolar Mine Events and Neutrino Anomaly," Phys. Lett. **58B**, 333 (1975). doi:10.1016/0370-2693(75)90667-X

[16] J. Preskill, "Subgroup Alignment in Hypercolor Theories," Nucl. Phys. B **177**, 21 (1981). doi:10.1016/0550-3213(81)90265-0

[17] L. J. Hall and A. E. Nelson, "Heavy Gluons and Monojets," Phys. Lett. **153B**, 430 (1985). doi:10.1016/0370-2693(85)90487-3

[18] J. Bagger, C. Schmidt and S. King, "Axigluon Production in Hadronic Collisions," Phys.

Rev. D **37**, 1188 (1988). doi:10.1103/PhysRevD.37.1188

[19] R. S. Chivukula, A. G. Cohen and E. H. Simmons, "New strong interactions at the Tevatron?," Phys. Lett. B **380**, 92 (1996) [hep-ph/9603311].

[20] E. H. Simmons, "Coloron phenomenology," Phys. Rev. D **55**, 1678 (1997) [hep-ph/9608269].

[21] Y. Bai and B. A. Dobrescu, "Heavy Octets and Tevatron Signals with Three or Four b Jets," JHEP **1107**, 100 (2011) [arXiv:1012.5814 [hep-ph]].

[22] R. S. Chivukula, A. Farzinnia, J. Ren and E. H. Simmons, "Constraints on the Scalar Sector of the Renormalizable Coloron Model," Phys. Rev. D **88**, no. 7, 075020 (2013) Erratum: [Phys. Rev. D **89**, no. 5, 059905 (2014)] [arXiv:1307.1064 [hep-ph]].

[23] R. S. Chivukula, A. Farzinnia, J. Ren and E. H. Simmons, "Hadron Collider Production of Massive Color-Octet Vector Bosons at Next-to-Leading Order," Phys. Rev. D **87**, no. 9, 094011 (2013) [arXiv:1303.1120 [hep-ph]].

[24] R. S. Chivukula, E. H. Simmons, A. Farzinnia and J. Ren, "LHC Constraints on a Higgs boson Partner from an Extended Color Sector," Phys. Rev. D **90**, no. 1, 015013 (2014) [arXiv:1404.6590 [hep-ph]].

[25] C. Y. Chen, A. Freitas, T. Han and K. S. M. Lee, "Heavy Color-Octet Particles at the LHC," JHEP **1505**, 135 (2015) [arXiv:1410.8113 [hep-ph]].

[26] R. S. Chivukula, A. Farzinnia and E. H. Simmons, "Vacuum Stability and Triviality Analyses of the Renormalizable Coloron Model," Phys. Rev. D **92**, no. 5, 055002 (2015) [arXiv:1504.03012 [hep-ph]].

[27] Y. Bai and B. A. Dobrescu, "Minimal $SU(3) \times SU(3)$ Symmetry Breaking Patterns," Phys. Rev. D **97**, no. 5, 055024 (2018) [arXiv:1710.01456 [hep-ph]].

[28] P. Agrawal and K. Howe, "Factoring the Strong CP Problem," JHEP **1812**, 029 (2018) [arXiv:1710.04213 [hep-ph]].

[29] Y. Bai and B. A. Dobrescu, "Collider Tests of the Renormalizable Coloron Model," JHEP **1804**, 114 (2018) [arXiv:1802.03005 [hep-ph]].

[30] Y. Bai, S. Lu and Q. F. Xiang, "Hexapod Coloron at the LHC," JHEP **1808**, 200 (2018) [arXiv:1805.09815 [hep-ph]].

[31] S. P. Martin, "Mixed gluinos and sgluons from a new $SU(3)$ gauge group," Phys. Rev. D **101**, no. 3, 035019 (2020) [arXiv:1912.01213 [hep-ph]].

[32] C. T. Hill, "Topcolor: Top quark condensation in a gauge extension of the standard model," Phys. Lett. B **266**, 419 (1991). doi:10.1016/0370-2693(91)91061-Y

[33] S. P. Martin, "Renormalizable top quark condensate models," Phys. Rev. D **45**, 4283 (1992). doi:10.1103/PhysRevD.45.4283, "A Tumbling top quark condensate model," Phys. Rev. D **46**, 2197 (1992) [hep-ph/9204204].

[34] C. T. Hill and S. J. Parke, "Top production: Sensitivity to new physics," Phys. Rev. D **49**, 4454 (1994) [hep-ph/9312324].

[35] B. A. Dobrescu and C. T. Hill, "Electroweak symmetry breaking via top condensation seesaw," Phys. Rev. Lett. **81**, 2634 (1998) [hep-ph/9712319].

[36] R. S. Chivukula, B. A. Dobrescu, H. Georgi and C. T. Hill, "Top Quark Seesaw Theory of Electroweak Symmetry Breaking," Phys. Rev. D **59**, 075003 (1999) [hep-ph/9809470].

[37] J. L. Hewett and T. G. Rizzo, "Low-Energy Phenomenology of Superstring Inspired E(6) Models," Phys. Rept. **183**, 193 (1989). doi:10.1016/0370-1573(89)90071-9

[38] E. Eichten, I. Hinchliffe, K. D. Lane and C. Quigg, "Super Collider Physics," Rev. Mod. Phys. **56**, 579 (1984) Addendum: [Rev. Mod. Phys. **58**, 1065 (1986)]. doi:10.1103/RevModPhys.56.579, 10.1103/RevModPhys.58.1065

[39] B. A. Dobrescu and F. Yu, "Coupling-Mass Mapping of Dijet Peak Searches," Phys. Rev. D **88**, no. 3, 035021 (2013) Erratum: [Phys. Rev. D **90**, no. 7, 079901 (2014)] [arXiv:1306.2629 [hep-ph]].

[40] U. Baur, I. Hinchliffe and D. Zeppenfeld, "Excited Quark Production at Hadron Colliders," Int. J. Mod. Phys. A **2**, 1285 (1987). doi:10.1142/S0217751X87000661

[41] U. Baur, M. Spira and P. M. Zerwas, "Excited Quark and Lepton Production at Hadron Colliders," Phys. Rev. D **42**, 815 (1990). doi:10.1103/PhysRevD.42.815

[42] L. A. Anchordoqui, H. Goldberg, D. Lust, S. Nawata, S. Stieberger and T. R. Taylor, "Dijet signals for low mass strings at the LHC," Phys. Rev. Lett. **101**, 241803 (2008) [arXiv:0808.0497 [hep-ph]].

[43] S. Cullen, M. Perelstein and M. E. Peskin, "TeV strings and collider probes of large extra dimensions," Phys. Rev. D **62**, 055012 (2000) [hep-ph/0001166].

[44] C. T. Hill and E. H. Simmons, "Strong Dynamics and Electroweak Symmetry Breaking," Phys. Rept. **381**, 235 (2003) Erratum: [Phys. Rept. **390**, 553 (2004)] [hep-ph/0203079].

[45] B. A. Dobrescu, K. Kong and R. Mahbubani, "Leptons and Photons at the LHC: Cascades through Spinless Adjoints," JHEP **0707**, 006 (2007) [hep-ph/0703231 [HEP-PH]].

[46] B. A. Dobrescu, K. Kong and R. Mahbubani, "Massive color-octet bosons and pairs of resonances at hadron colliders," Phys. Lett. B **670**, 119 (2008) [arXiv:0709.2378 [hep-ph]].

[47] L. Randall and R. Sundrum, "An Alternative to compactification," Phys. Rev. Lett. **83**, 4690 (1999) [hep-th/9906064].

[48] T. Han, J. D. Lykken and R. J. Zhang, "On Kaluza-Klein states from large extra dimensions," Phys. Rev. D **59**, 105006 (1999) [hep-ph/9811350].

[49] M. Chala, F. Kahlhoefer, M. McCullough, G. Nardini and K. Schmidt-Hoberg, "Constraining Dark Sectors with Monojets and Dijets," JHEP **1507**, 089 (2015) [arXiv:1503.05916 [hep-ph]].

[50] D. Abercrombie *et al.*, "Dark Matter Benchmark Models for Early LHC Run-2 Searches: Report of the ATLAS/CMS Dark Matter Forum," Phys. Dark Univ. **26**, 100371 (2019) [arXiv:1507.00966 [hep-ex]].

[51] J. Abdallah *et al.*, "Simplified Models for Dark Matter Searches at the LHC," Phys. Dark Univ. **9-10**, 8 (2015) [arXiv:1506.03116 [hep-ph]].

[52] A. Boveia *et al.*, "Recommendations on presenting LHC searches for missing transverse energy signals using simplified s-channel models of dark matter," Phys. Dark Univ. **27**, 100365 (2020) [arXiv:1603.04156 [hep-ex]].

[53] T. Han, I. Lewis and Z. Liu, "Colored Resonant Signals at the LHC: Largest Rate and Simplest Topology," JHEP **1012**, 085 (2010) [arXiv:1010.4309 [hep-ph]].

[54] S. Mukherjee [CMS Collaboration], "Data Scouting : A New Trigger Paradigm," arXiv:1708.06925 [hep-ex].

[55] S. P. Martin, "Signal-background interference for a singlet spin-0 digluon resonance at the LHC," Phys. Rev. D **94**, no. 3, 035003 (2016) [arXiv:1606.03026 [hep-ph]].

[56] D. A. Dicus and S. S. D. Willenbrock, "Photon Pair Production and the Intermediate Mass Higgs Boson," Phys. Rev. D **37**, 1801 (1988). doi:10.1103/PhysRevD.37.1801

[57] L. J. Dixon and M. S. Siu, "Resonance continuum interference in the diphoton Higgs signal at the LHC," Phys. Rev. Lett. **90**, 252001 (2003) [hep-ph/0302233].

[58] S. P. Martin, "Shift in the LHC Higgs Diphoton Mass Peak from Interference with Background," Phys. Rev. D **86**, 073016 (2012) [arXiv:1208.1533 [hep-ph]].

[59] D. de Florian, N. Fidanza, R.J. Hernandez-Pinto, J. Mazzitelli, Y. Rotstein Habarnau and G.F.R. Sborlini, "A complete $O(\alpha_S^2)$ calculation of the signal-background interference for the Higgs diphoton decay channel," Eur. Phys. J. C **73**, no.4, 2387 (2013) [arXiv:1303.1397 [hep-ph]].

[60] S. P. Martin, "Interference of Higgs Diphoton Signal and Background in Production with a Jet at the LHC," Phys. Rev. D **88**, no. 1, 013004 (2013) [arXiv:1303.3342 [hep-ph]].

[61] L. J. Dixon and Y. Li, "Bounding the Higgs Boson Width Through Interferometry," Phys. Rev. Lett. **111**, 111802 (2013) [arXiv:1305.3854 [hep-ph]].

[62] F. Coradeschi, D. de Florian, L. J. Dixon, N. Fidanza, S. Hche, H. Ita, Y. Li and J. Mazzitelli, "Interference effects in the $H(\to \gamma\gamma) + 2$ jets channel at the LHC," Phys. Rev. D **92**, no. 1, 013004 (2015) [arXiv:1504.05215 [hep-ph]].

[63] C. P. Becot, "Diphoton lineshape of the BEH boson using the ATLAS detector at the LHC: calibration, mass, width and interferences," CERN-THESIS-2015-193, LAL-15-303.

[64] J. Campbell, M. Carena, R. Harnik and Z. Liu, "Interference in the $gg \to h \to \gamma\gamma$ On-Shell Rate and the Higgs Boson Total Width," Phys. Rev. Lett. **119** (2017) no.18, 181801 [arXiv:1704.08259 [hep-ph]].

[65] L. Cieri, F. Coradeschi, D. de Florian and N. Fidanza, "Transverse-momentum resummation for the signal-background interference in the $H \to \gamma\gamma$ channel at the LHC," Phys. Rev. D **96** (2017) no.5, 054003 [arXiv:1706.07331 [hep-ph]].

[66] E. W. N. Glover and J. J. van der Bij, "Vector Boson Pair Production Via Gluon Fusion," Phys. Lett. B **219**, 488 (1989). doi:10.1016/0370-2693(89)91099-X

[67] E. W. N. Glover and J. J. van der Bij, "Z Boson Pair Production Via Gluon Fusion," Nucl. Phys. B **321**, 561 (1989). doi:10.1016/0550-3213(89)90262-9

[68] M. H. Seymour, "The Higgs boson line shape and perturbative unitarity," Phys. Lett. B **354**, 409 (1995) [hep-ph/9505211].

[69] T. Binoth, M. Ciccolini, N. Kauer and M. Kramer, "Gluon-induced W-boson pair production at the LHC," JHEP **0612**, 046 (2006) [hep-ph/0611170].

[70] E. Accomando, "The Process $gg \to WW$ as a probe into the EWSB mechanism," Phys. Lett. B **661**, 129 (2008) [arXiv:0709.1364 [hep-ph]].

[71] J. M. Campbell, R. K. Ellis and C. Williams, "Gluon-Gluon Contributions to W^+W^- Production and Higgs Interference Effects," JHEP **1110**, 005 (2011) [arXiv:1107.5569 [hep-ph]].

[72] N. Kauer, "Signal-background interference in $gg \to H \to VV$," PoS RADCOR **2011**, 027 (2011) [arXiv:1201.1667 [hep-ph]].

[73] G. Passarino, "Higgs Interference Effects in $gg \to ZZ$ and their Uncertainty," JHEP **1208**, 146 (2012) [arXiv:1206.3824 [hep-ph]].

[74] N. Kauer and G. Passarino, "Inadequacy of zero-width approximation for a light Higgs boson signal," JHEP **1208**, 116 (2012) [arXiv:1206.4803 [hep-ph]]. N. Kauer, "Inadequacy of zero-width approximation for a light Higgs boson signal," Mod. Phys. Lett. A **28** (2013), 1330015 [arXiv:1305.2092 [hep-ph]].

[75] F. Campanario, Q. Li, M. Rauch and M. Spira, "ZZ+jet production via gluon fusion at the LHC," JHEP **1306**, 069 (2013) [arXiv:1211.5429 [hep-ph]].

[76] M. Bonvini, F. Caola, S. Forte, K. Melnikov and G. Ridolfi, "Signal-background interference effects for $gg \to H \to W^+W^-$ beyond leading order," Phys. Rev. D **88**, no. 3, 034032 (2013) [arXiv:1304.3053 [hep-ph]].

[77] F. Caola and K. Melnikov, "Constraining the Higgs boson width with ZZ production at the LHC," Phys. Rev. D **88**, 054024 (2013) [arXiv:1307.4935 [hep-ph]].

[78] J. M. Campbell, R. K. Ellis and C. Williams, "Bounding the Higgs Width at the LHC Using Full Analytic Results for $gg \to e^-e^+\mu^-\mu^+$," JHEP **04** (2014), 060 [arXiv:1311.3589 [hep-ph]].

[79] M. Chen, T. Cheng, J. S. Gainer, A. Korytov, K. T. Matchev, P. Milenovic, G. Mitselmakher, M. Park, A. Rinkevicius and M. Snowball, "The role of interference in unraveling the ZZ-couplings of the newly discovered boson at the LHC," Phys. Rev. D **89** (2014) no.3, 034002 [arXiv:1310.1397 [hep-ph]].

[80] N. Kauer, "Interference effects for H $\to$ WW/ZZ $\to \ell\bar{\nu}_\ell\bar{\ell}\nu_\ell$ searches in gluon fusion at the LHC," JHEP **12** (2013), 082 [arXiv:1310.7011 [hep-ph]].

[81] J. M. Campbell, R. K. Ellis and C. Williams, "Bounding the Higgs Width at the LHC: Complementary Results from $H \to WW$," Phys. Rev. D **89** (2014) no.5, 053011 [arXiv:1312.1628 [hep-ph]].

[82] C. Englert and M. Spannowsky, "Limitations and Opportunities of Off-Shell Coupling Measurements," Phys. Rev. D **90** (2014), 053003 [arXiv:1405.0285 [hep-ph]].

[83] J. M. Campbell, R. K. Ellis, E. Furlan and R. Röntsch, "Interference effects for Higgs boson mediated Z-pair plus jet production," Phys. Rev. D **90**, no. 9, 093008 (2014) [arXiv:1409.1897].

[84] C. Englert, Y. Soreq and M. Spannowsky, "Off-Shell Higgs Coupling Measurements in BSM scenarios," JHEP **05** (2015), 145 [arXiv:1410.5440 [hep-ph]].

[85] H. E. Logan, "Hiding a Higgs width enhancement from off-shell $gg(\to h^*) \to ZZ$ measurements," Phys. Rev. D **92**, no. 7, 075038 (2015) [arXiv:1412.7577 [hep-ph]].

[86] N. Kauer, "Off-shell Higgs signal and total width determination at the LHC," PoS **FFP14** (2016), 114 [arXiv:1502.02581 [hep-ph]].

[87] C. S. Li, H. T. Li, D. Y. Shao and J. Wang, "Soft gluon resummation in the signal-background interference process of $gg(\to h^*) \to ZZ$," JHEP **08** (2015), 065 [arXiv:1504.02388 [hep-ph]].

[88] V. Khachatryan *et al.* [CMS Collaboration], "Constraints on the Higgs boson width from off-shell production and decay to Z-boson pairs," Phys. Lett. B **736**, 64 (2014) [arXiv:1405.3455 [hep-ex]].

[89] G. Aad *et al.* [ATLAS Collaboration], "Constraints on the off-shell Higgs boson signal strength in the high-mass ZZ and WW final states with the ATLAS detector," Eur. Phys. J. C **75**, no. 7, 335 (2015) [arXiv:1503.01060 [hep-ex]].

[90] V. Khachatryan *et al.* [CMS], "Limits on the Higgs boson lifetime and width from its decay

to four charged leptons," Phys. Rev. D **92** (2015) no.7, 072010 [arXiv:1507.06656 [hep-ex]].

[91] V. Khachatryan *et al.* [CMS Collaboration], "Search for Higgs boson off-shell production in proton-proton collisions at 7 and 8 TeV and derivation of constraints on its total decay width," JHEP **1609**, 051 (2016) [arXiv:1605.02329 [hep-ex]].

[92] M. Aaboud *et al.* [ATLAS], "Constraints on off-shell Higgs boson production and the Higgs boson total width in $ZZ \to 4\ell$ and $ZZ \to 2\ell2\nu$ final states with the ATLAS detector," Phys. Lett. B **786** (2018), 223-244 [arXiv:1808.01191 [hep-ex]].

[93] A. M. Sirunyan *et al.* [CMS], "Measurements of the Higgs boson width and anomalous HVV couplings from on-shell and off-shell production in the four-lepton final state," Phys. Rev. D **99** (2019) no.11, 112003 [arXiv:1901.00174 [hep-ex]].

[94] E. Boos, V. Bunichev, L. Dudko and M. Perfilov, "Interference between W' and W in single-top quark production processes," Phys. Lett. B **655**, 245 (2007) [hep-ph/0610080]. T. G. Rizzo, "The Determination of the Helicity of W' Boson Couplings at the LHC," JHEP **0705**, 037 (2007) [arXiv:0704.0235 [hep-ph]]. A. Papaefstathiou and O. Latunde-Dada, "NLO production of W' bosons at hadron colliders using the MC@NLO and POWHEG methods," JHEP **0907**, 044 (2009) [arXiv:0901.3685]. E. Accomando, D. Becciolini, S. De Curtis, D. Dominici, L. Fedeli and C. Shepherd-Themistocleous, "Interference effects in heavy W'-boson searches at the LHC," Phys. Rev. D **85**, 115017 (2012) [arXiv:1110.0713 [hep-ph]]. L. Bian, D. Liu, J. Shu and Y. Zhang, "Interference Effect on Resonance Studies in Searches of Heavy Particles," Int. J. Mod. Phys. **31**, no. 14n15, 1650083 (2016) [arXiv:1509.02787].

[95] E. Accomando, D. Becciolini, A. Belyaev, S. Moretti and C. Shepherd-Themistocleous, "Z' at the LHC: Interference and Finite Width Effects in Drell-Yan," JHEP **1310**, 153 (2013) [arXiv:1304.6700 [hep-ph]]. E. Accomando, D. Barducci, S. De Curtis, J. Fiaschi, S. Moretti and C. H. Shepherd-Themistocleous, "Drell-Yan production of multi Z'-bosons at the LHC within Non-Universal ED and 4D Composite Higgs Models," arXiv:1602.05438 [hep-ph].

[96] D. Dicus, A. Stange and S. Willenbrock, "Higgs decay to top quarks at hadron colliders," Phys. Lett. B **333**, 126 (1994) [hep-ph/9404359]. D. Choudhury, R. M. Godbole, R. K. Singh and K. Wagh, "Top production at the Tevatron/LHC and nonstandard, strongly interacting spin one particles," Phys. Lett. B **657**, 69 (2007) [0705.1499 [hep-ph]]. A. Djouadi, G. Moreau and R. K. Singh, "Kaluza-Klein excitations of gauge bosons at the LHC," Nucl. Phys. B **797**, 1 (2008) [0706.4191 [hep-ph]]. R. Frederix and F. Maltoni, "Top pair invariant mass distribution: A Window on new physics," JHEP **0901**, 047 (2009) [0712.2355 [hep-ph]]. U. Haisch and S. Westhoff, "Massive Color-Octet Bosons: Bounds on Effects in Top-Quark Pair Production," JHEP **1108**, 088 (2011) [1106.0529 [hep-ph]]. N. Craig, F. D'Eramo, P. Draper, S. Thomas and H. Zhang, "The Hunt for the Rest of the Higgs Bosons," JHEP **1506**, 137 (2015) [1504.04630 [hep-ph]]. B. Hespel, F. Maltoni and E. Vryonidou, "Signal background interference effects in heavy scalar production and decay to a top-anti-top pair," JHEP **10** (2016), 016 [arXiv:1606.04149 [hep-ph]]. M. Carena and Z. Liu, "Challenges and opportunities for heavy scalar searches in the $t\bar{t}$ channel at the LHC," JHEP **11** (2016), 159 [arXiv:1608.07282 [hep-ph]]. A. Djouadi, J. Ellis and J. Quevillon, "Interference effects in the decays of spin-zero resonances into $\gamma\gamma$ and $t\bar{t}$," JHEP **1607**, 105 (2016) [arXiv:1605.00542 [hep-ph]]. A. Djouadi, J. Ellis, A. Popov and J. Quevillon, "Interference effects in $t\bar{t}$ production at the LHC as a window on new physics," JHEP **03** (2019), 119 [arXiv:1901.03417 [hep-ph]].

[97] S. Jung, Y. W. Yoon and J. Song, "Interference effect on a heavy Higgs resonance signal in the $\gamma\gamma$ and ZZ channels," Phys. Rev. D **93**, no. 5, 055035 (2016) [arXiv:1510.03450 [hep-ph]].

[98] S. Jung, J. Song and Y. W. Yoon, "Dip or nothingness of a Higgs resonance from the interference with a complex phase," Phys. Rev. D **92** (2015) no.5, 055009 [arXiv:1505.00291 [hep-ph]].

[99] N. Craig, S. Renner and D. Sutherland, "Exploring Peaks and Valleys in the Diphoton Spectrum," Phys. Rev. D **94** (2016) no.7, 075011 [arXiv:1607.06074 [hep-ph]].

[100] N. Kauer, A. Lind, P. Maierhofer and W. Song, "Higgs interference effects at the one-loop level in the 1-Higgs-Singlet extension of the Standard Model," JHEP **07** (2019), 108 [arXiv:1905.03296 [hep-ph]].

[101] D. Choudhury, R. M. Godbole and P. Saha, "Dijet resonances, widths and all that," JHEP **01**, 155 (2012) doi:10.1007/JHEP01(2012)155 [arXiv:1111.1054 [hep-ph]].

[102] J. P. Ma, J. X. Wang and S. Zhao, "Breakdown of QCD Factorization for P-Wave Quarkonium Production at Low Transverse Momentum," Phys. Lett. B **737**, 103 (2014) [arXiv:1405.3373 [hep-ph]].

[103] W. Beenakker, R. Kleiss and G. Lustermans, "No Landau-Yang in QCD," arXiv:1508.07115 [hep-ph].

[104] M. Cacciari, L. Del Debbio, J. R. Espinosa, A. D. Polosa and M. Testa, "A note on the fate of the Landau-Yang theorem in non-Abelian gauge theories," Phys. Lett. B **753**, 476 (2016) [arXiv:1509.07853 [hep-ph]].

[105] Y. Bai and W. Y. Keung, "Can vanishing mass-on-shell interactions generate a dip at colliders?," Int. J. Mod. Phys. A **30**, no. 20, 1550120 (2015) [arXiv:1407.6355 [hep-ph]].

[106] M. D. Schwartz, "Quantum Field Theory and the Standard Model," Cambridge University Press, 2014.

[107] K. Hagiwara, J. Kanzaki, Q. Li and K. Mawatari, "HELAS and MadGraph/MadEvent with spin-2 particles," Eur. Phys. J. C **56**, 435 (2008) [arXiv:0805.2554 [hep-ph]].

[108] G. F. Giudice, R. Rattazzi and J. D. Wells, "Quantum gravity and extra dimensions at high-energy colliders," Nucl. Phys. B **544**, 3 (1999) [hep-ph/9811291].

[109] H. E. Haber, "Useful relations among the generators in the defining and adjoint representations of $SU(N)$," arXiv:1912.13302 [math-ph].

[110] A. J. MacFarlane, A. Sudbery and P. H. Weisz, "On Gell-Mann's lambda-matrices, d- and f-tensors, octets, and parametrizations of SU(3)," Commun. Math. Phys. **11**, 77 (1968). doi:10.1007/BF01654302

[111] R. D. Ball *et al.* [NNPDF Collaboration], "Parton distributions with QED corrections," Nucl. Phys. B **877**, 290 (2013) [arXiv:1308.0598 [hep-ph]].

[112] T. Sjostrand, S. Mrenna and P. Z. Skands, "PYTHIA 6.4 Physics and Manual," JHEP **0605**, 026 (2006) [hep-ph/0603175].

[113] T. Sjostrand et al., "An Introduction to PYTHIA 8.2," Comput. Phys. Commun. **191**, 159 (2015) [hep-ph/1410.3012].

[114] J. de Favereau *et al.* [DELPHES 3 Collaboration], "DELPHES 3, A modular framework for fast simulation of a generic collider experiment," JHEP **1402**, 057 (2014) [arXiv:1307.6346 [hep-ex]].

[115] J. Alwall, M. Herquet, F. Maltoni, O. Mattelaer and T. Stelzer, "MadGraph 5 : Going Beyond," JHEP **1106**, 128 (2011) [1106.0522].

[116] A. Alloul, N. D. Christensen, C. Degrande, C. Duhr and B. Fuks, "FeynRules 2.0 - A complete toolbox for tree-level phenomenology," Comput. Phys. Commun. **185**, 2250 (2014) [arXiv:1310.1921 [hep-ph]].

[117] E. Boos *et al.*, "Generic User Process Interface for Event Generators," hep-ph/0109068.

[118] F. Maltoni, K. Paul, T. Stelzer and S. Willenbrock, "Color Flow Decomposition of QCD Amplitudes," Phys. Rev. D **67**, 014026 (2003) doi:10.1103/PhysRevD.67.014026 [hep-ph/0209271].

[119] M. E. Peskin, "How to turn a hep-ph paper into a simulation," West Coast LHC Theory Network, UC Irvine meeting, May 4, 2007.

[120] J. H. Collins, K. Howe and B. Nachman, "Extending the search for new resonances with machine learning," Phys. Rev. D **99**, no. 1, 014038 (2019) [arXiv:1902.02634 [hep-ph]].

[121] B. G. Lillard, T. Plehn, A. Romero and T. Tait, M.P., "Multi-scale Mining of Kinematic Distributions with Wavelets," SciPost Phys. **8** (2020) no.3, 043 [arXiv:1906.10890 [hep-ph]].

[122] H. Beauchesne and Y. Kats, "Searching for periodic signals in kinematic distributions using continuous wavelet transforms," Eur. Phys. J. C **80** (2020) no.3, 192 arXiv:1907.03676 [hep-ph].

[123] B. Nachman and D. Shih, "Anomaly Detection with Density Estimation," arXiv:2001.04990 [hep-ph].

[124] A. Andreassen, B. Nachman and D. Shih, "Simulation Assisted Likelihood-free Anomaly Detection," arXiv:2001.05001 [hep-ph].